Atmos. Chem. Phys. Discuss., 8, 20051–20112, 2008
www.atmos-chem-phys-discuss.net/8/20051/2008/

Atmospheric Chemistry and Physics Discussions

This discussion paper is/has been under review for the journal *Atmospheric Chemistry and Physics (ACP)*. Please refer to the corresponding final paper in *ACP* if available.

Carbon source/sink information provided by column CO_2 measurements from the Orbiting Carbon Observatory

D. F. Baker[1,*], **H. Bösch**[2], **S. C. Doney**[1], **and D. S. Schimel**[3]

[1]Department of Marine Chemistry and Geochemistry, Woods Hole Oceanographic Institution, Woods Hole, MA 02543-1543, USA
[2]Department of Physics, University of Leicester, University Road, Leicester, LE1 7RH, UK
[3]National Ecological Observatory Network, Inc., 3223 Arapahoe Ave. Suite 210, Boulder, CO 80303, USA
[*]now at: Cooperative Institute for Research in the Atmosphere, Colorado State University, Fort Collins, CO 80523-1375, USA

Received: 21 August 2008 – Accepted: 30 September 2008 – Published: 28 November 2008

Correspondence to: D. F. Baker (baker@cira.colostate.edu)

Published by Copernicus Publications on behalf of the European Geosciences Union.

Abstract

We perform a series of observing system simulation experiments (OSSEs) to quantify how well surface CO_2 fluxes may be estimated using column-integrated CO_2 data from the Orbiting Carbon Observatory (OCO), given the presence of various error sources. We use variational data assimilation to optimize weekly fluxes at $2^\circ \times 5^\circ$ (lat/lon) using simulated data averaged only across the ~33 s that OCO takes to cross a typical $2^\circ \times 5^\circ$ model grid box. Grid-scale OSSEs of this sort have been carried out before for OCO using simplified assumptions for the measurement error. Here, we more accurately describe the OCO measurements in two ways. First, we use new estimates of the single-sounding retrieval uncertainty and averaging kernel, both computed as a function of surface type, solar zenith angle, aerosol optical depth, and pointing mode (nadir vs. glint). Second, we collapse the information content of all valid retrievals from each grid box crossing into an equivalent multi-sounding measurement uncertainty, factoring in both time/space error correlations and data availability due to clouds and thick aerosols (calculated from MODIS data). Finally, we examine the impact of three types of systematic errors: measurement biases due to aerosols, transport errors, and errors caused by assuming incorrect error statistics.

When only random measurement errors are considered, both nadir- and glint-mode data give error reductions of ~50% over the land for the weekly fluxes, and ~65% for seasonal fluxes. Systematic errors reduce both the magnitude and extent of these improvements by up to a factor of two, however. Flux improvements over the ocean are significant only when using glint-mode data and are smaller than those over land; when the assimilation is mistuned, slow convergence makes even these improvements difficult to achieve. The OCO data may prove most useful over the tropical land areas, where our current flux knowledge is weak and where the measurements remain fairly accurate even in the face of systematic errors.

ACPD

8, 20051–20112, 2008

1 Introduction

By themselves, the well-calibrated, long-term atmospheric CO_2 measurements at Mauna Loa and the South Pole have revealed much of what we know of the functioning of the global carbon cycle: the steady rise of global CO_2 concentrations driven by anthropogenic fossil fuel burning, the uptake of about half this input by sinks in the oceans and on land, and interannual variability in these sinks that is correlated with El Niño events and large volcanic eruptions. However, to understand why the carbon cycle responds as it does to the climatic and anthropogenic forcing, and to be able to predict how it will behave in the future, models are needed of the important biogeochemical processes in both the oceans and land biosphere. These process models are tuned to agree with data from local study sites, then scaled up to give surface CO_2 fluxes globally. When run through atmospheric transport models, these fluxes yield atmospheric CO_2 concentrations that may be compared to CO_2 measurements and used to test and improve the flux models. Atmospheric inverse methods provide a framework for optimizing parameters in the process models or the surface CO_2 fluxes they produce.

So far, the "top-down" atmospheric inverse approach to validating carbon models has been only marginally successful: where the data are most dense, fluxes may be estimated at continental scales (Baker et al., 2006a), but not at the regional scales needed to provide insight into flaws in the carbon models. Part of the problem is that the transport models have systematic mixing errors, including between hemispheres and out of the planetary boundary layer. The models also have great difficulty representing point measurements, particularly over the continents, using grid boxes 100s of km long on a side. The largest problem, however, is that the spatio-temporal density of the current measurement network is insufficient to correct the surface fluxes at regional scales. For the continental United States, for example, solving for fluxes at a 500 km resolution would require at least 7 500 000 km^2/(500 km)^2≈30 sites, each sampling air high enough in the column to have a footprint at least 500 km on a side (to avoid

ACPD
8, 20051–20112, 2008

corrections occurring just in the immediate vicinity of the measurement sites) with a frequency dictated by the cross-continental advection time scale.

Space-based measurements provide the most realistic opportunity to achieve coverage at such regional scales. Two satellites specifically designed to measure the column-averaged dry air mole fraction of CO_2 (X_{CO_2}) will be launched soon: NASA's Orbiting Carbon Observatory (OCO) and the Japanese Greenhouse Gases Observing Satellite (GOSAT). Their instruments measure CO_2 absorption in the near infra-red (IR) portion of the reflected solar beam and thus have sensitivity down to the surface, which is required to observe the variable near-surface CO_2 concentrations most affected by the fluxes (Olsen and Randerson, 2004). Previous instruments that sensed CO_2 emission in thermal IR bands had sensitivity mainly in the mid- to upper-troposphere and provided less information about the surface fluxes (Chevallier et al., 2005a, b). Both OCO and GOSAT are in sun-synchronous orbits with early afternoon sun-lit equator crossing times and inclinations of 98°. OCO's field of view (FOV), ~2 km on a side, was chosen that small on purpose, to increase the chances of seeing through holes in the clouds, whose radiative transfer effects decrease the accuracy of the X_{CO_2} retrieval algorithm (Crisp et al., 2004). OCO has a maximum cross-track scan width of only ~10 km; these thin scans are spaced every 25° in longitude, 99 min apart. In addition to nominal near-nadir pointing, both missions can also point at the sun glint spot; this greatly increases the signal over the oceans, which do not otherwise provide much reflection in the near infrared (Miller et al., 2007). The coverage of the satellite data is still limited, though. Neither mission collects data at night, and they provide very little information on the diurnal cycle of CO_2 since they sample only in the local early afternoon. The 25° in longitude separating subsequent OCO passes is large enough to make it difficult to resolve synoptic scale variability; GOSAT scans across track, so should do better. Finally, both missions will probably have to remove a variety of biases (Miller et al., 2007), especially those related to aerosols and thin clouds, before their measurement accuracy will meet their design goals. Future satellite missions that follow OCO and GOSAT should be able to sense over the night side of the Earth using

ACPD
8, 20051–20112, 2008

active sensors (e.g. lidar); more complete spatio-temporal coverage could be achieved by placing scanning sensors aboard a constellation of geosynchronous satellites.

In this study, we quantify how well X_{CO_2} measurements from OCO will help estimate sources and sinks of CO_2 at the surface. We use a tracer transport model to relate patterns in simulated atmospheric CO_2 concentration measurements to the surface CO_2 fluxes at earlier times that determined them. Due to atmospheric mixing, measurements at progressively higher layers in the atmospheric column reflect fluxes from increasing broad areas at the surface. The transport model allows this X_{CO_2} measurement information, weighted properly in the vertical column, to be distributed appropriately to fill in the 25° gaps between subsequent OCO passes on any given day. Though OCO cannot clarify the diurnal cycle of flux, it can properly account for variability due to synoptic-scale weather systems when they are modeled well by the transport model. Transport models have often been used in back-trajectory inversions to solve for local fluxes with in situ measurements from aircraft campaigns (Gerbig et al., 2003; Lin et al., 2004). For the more regularly-distributed global flask network, flux inversions based on the "Bayesian synthesis" approach (Enting et al., 1995) have been favored. This method has also been used to determine the information on surface CO_2 fluxes provided by satellite data (Rayner and O'Brien, 2001; Houweling et al., 2004; Miller et al., 2007), although only for monthly fluxes from fairly large emission regions (~2000 km on a side) since the number of fluxes solved for was limited by the inversion method. The density of OCO's data should permit fluxes to be estimated at a finer resolution than this, however.

We solve for the CO_2 fluxes at a 2°×5° resolution (lat/lon) using a state-of-the-art variational data assimilation scheme (Baker et al., 2006b); optimized time-varying 3-D CO_2 concentration fields are also produced as a by-product. The fluxes are solved at a weekly resolution, though the measurements are modeled at the time step of the transport model (1 h). Our data assimilation approach is used to perform observing system simulation experiments (OSSEs), in which simulated data and measurement errors are input to produce statistics on the flux estimation errors and the improvement in the ini-

ACPD
8, 20051–20112, 2008

tial guess of the fluxes. Both Baker et al. (2006b) and Chevallier et al. (2007a) have done preliminary OSSEs for OCO using this approach before. For measurements, they assumed a single measurement per model grid box with a 1 or 2 ppm uncertainty value (1σ), respectively, and with a flat weighting versus pressure in the vertical. Here, we improve upon their assumptions in two ways. First, for each individual retrieval, we use new OCO X_{CO_2} retrieval uncertainties and averaging kernels (AKs) calculated as a function of surface type, solar zenith angle, aerosol optical depth (OD), and pointing mode (nadir vs. glint) using the OCO Level 2 X_{CO_2} retrieval scheme forced with radiances simulated by the OCO "full-physics" radiative transfer scheme, taken from Bösch et al. (2008). Second, instead of assuming only a single valid retrieval per crossing of each model grid box (takes ~33 s for our $2^\circ \times 5^\circ$ boxes), we collapse the information content of all valid retrievals across each ~33 s grid box crossing into an equivalent multi-sounding measurement uncertainty, which is then used in the assimilation. Valid X_{CO_2} retrievals are only attempted for cloud-free conditions in which the aerosol OD is less than 0.30, in order to reduce radiative transfer errors due to scattering. We compute the number of valid retrievals for each grid box crossing based on the probability that such cloud-free and low-aerosol conditions exist for each retrieval; these probabilities are computed using climatological statistics from MODIS data. We attempt to account for along-track correlations in the X_{CO_2} measurements when specifying the equivalent measurement uncertainty for each model grid box crossing. Finally, we examine more types of systematic errors than these previous studies: measurement biases due to aerosols, transport errors, and errors caused by "mistuning" the inversion (i.e., assuming incorrect a priori flux and measurement error statistics).

ACPD
8, 20051–20112, 2008

2 Method

2.1 OCO orbit and resolution choices

The OCO satellite measures X_{CO_2}, the column-averaged dry air mole fraction of CO_2, in the near-infrared (reflected solar bands) with sensitivity down to the surface, but with a vertical weighting that varies with surface type, aerosol amount, and solar zenith angle (SZA) as described in Bösch et al. (2008). It samples a single field of view of up to 2.7 km^2 every 40 ms over a ground track up to 10 km wide (Crisp et al., 2004). It is in a sun-synchronous orbit taking a single sun-lit pass of data per day at ~13:30 local time, with ~25° in longitude separating subsequent passes. (The local time of the ascending node was just recently changed to 13:30; here we use a 13:18 value specified earlier, but we do not expect this to significantly impact our results.) Examples of the sun-lit portion of the OCO FOV ground track are given in Fig. 1. The OCO ground track repeats precisely after 16 days, a fact that is useful for calibrating the measurements at fixed ground sites. However, as shown in Fig. 1, the ground tracks also achieve a somewhat uniform spatial coverage of ~3.5° in longitude after only 7 days. We will use this 7-day period here as the discretization step for our solved-for fluxes, since it gives good coverage over our transport model grid boxes, 5° wide in longitude. The latitudinal resolution of the model is chosen at 2° to match that of our meteorological products to give maximum resolution in the predominantly north/south (N/S) direction of the OCO ground tracks. Because the OCO data, occurring once per day locally, cannot shed much insight into the diurnal cycle of X_{CO_2}, some assumption for the diurnal cycle of the surface CO_2 fluxes must also be made (see Sect. 2.4 below); this then allows multi-day flux blocks to be estimated in a reasonable way from the data.

2.2 Transport model

An off-line atmospheric transport model (the Parameterized Chemical Transport Model, or PCTM; see Kawa et al., 2004) is used to relate surface CO_2 fluxes to CO_2 con-

ACPD
8, 20051–20112, 2008

centrations. It is driven by pre-calculated meteorological fields (horizontal winds, surface pressure, vertical diffusion coefficient, and cloud-convective mass flux) from the GEOS4-DAS reanalysis (Bloom et al., 2005) for the year 1987, interpolated from the resolution normally input to PCTM (2.0°×2.5° in lat/lon; 55 vertical layers) to the resolution of the model version used here (2°×5° lat/lon; 25 vertical layers). The model uses a vertically-Lagrangian finite volume advection scheme (Lin, 2004) and has simple linear schemes for both dry and convective vertical mixing. The 2°×5° horizontal resolution used here has the advantage of retaining the full N/S (mostly along-track) resolution of the original winds, while allowing for a relatively long (1 h) step size. Because the measurement information is already explicitly spread 5° in longitude (mainly across-track) due to the 2°×5° box size, no additional spatial correlations are assumed in this analysis.

The modeled 3-D concentration fields are sampled in as similar a manner to the true OCO X_{CO_2} measurements as the transport model permits: vertically, using the averaging kernels computed by Bösch et al. (2008), as a function of surface type, SZA, aerosol OD, and nadir or glint viewing mode; horizontally, at the transport model's 2°×5° resolution; and temporally, at the model's integration time step (1 h).

The adjoint of the transport model is needed in the assimilation scheme, to move model-data misfit information backwards in time to compute the cost function gradient direction. The adjoint of the forward model has been computed in an efficient manner by running a linear version of the forward advection scheme backwards, and by computing the exact adjoint of the vertical mixing schemes' column mixing matrices. As shown in Baker et al. (2006b), this adjoint is precise enough to allow the true fluxes to be recovered to within 0.2% after 60 iterations in a perfect model simulation with no measurement errors added.

2.3 Data assimilation scheme

We solve for weekly surface CO_2 fluxes at 2°x 5° in lat/lon, using X_{CO_2} measurements that are modeled also at 2°×5° across a data span of 1 year. We will do this over a

data span of 1 year. Both the number of fluxes to be solved for (90×72×52=~35 000) and the number of data values used (365×1500=~50 000) are at least an order of magnitude larger than that used in typical past time-dependent CO_2 inversions (e.g., Rödenbeck et al., 2003; Peylin et al., 2005b; Patra et al., 2005; Baker et al., 2006a; Rayner et al., 2008). Most of these previous inversions used the "Bayesian synthesis method", a batch least squares technique in which transport basis functions were constructed in separate model runs, either one for each solved-for flux or (backwards in time using the adjoint) one for each measurement, to fill a Jacobian matrix relating fluxes to concentrations. The resulting system of linear equations was solved directly to give both the optimal estimate and the accompanying covariance matrix describing the estimation errors. For problems of the size addressed here, it is not computationally feasible to use this sort of direct method – a more computationally efficient approach is needed.

We have chosen to use a variational data assimilation approach to overcome these hurdles. It is similar to the "4-D Var" methods used in numerical weather prediction, except that instead of optimizing an initial condition (the atmospheric state) at the start of a relatively short assimilation window, we optimize time-varying boundary values (surface CO_2 fluxes) over a longer measurement span. Baker et al. (2006b) outline the mathematical details and give some test results using simulated data. Rödenbeck (2005) has used a similar approach to estimate monthly CO_2 fluxes from 20+ years of in situ CO_2 measurements, and Meirink et al. (2008) have recently used this method to estimate surface CH_4 fluxes on a fine grid from SCIAMACHY data. Rayner et al. (2005) have used a variational approach for solve directly for parameters in land biosphere carbon models, bypassing the surface fluxes. Over the past several years, a new class of ensemble filtering methods have also been applied to the tracer transport problem (Peters et al., 2005; Zupanski et al., 2007). Both the ensemble and variational methods achieve their computational savings in a similar fashion: by solving for only an approximate, low-rank version of the full covariance matrix. A key advantage of the ensemble filters, however, is that they may be able to achieve

ACPD
8, 20051–20112, 2008

computational savings as great as the variational methods without needing to use the adjoint to the atmospheric transport model (which is often costly to develop). This may be done, for example, using the ensemble version of a fixed lag Kalman smoother, at the cost of inverting a matrix at each time step whose size is related to the number of parameters estimated across the smoother's sliding time window. While the ensemble methods hold out great promise for the future, we have chosen to go with the proven computational savings of the variational methods for this study.

The variational method works in an iterative fashion, running an estimate of the surface fluxes forward in time through the transport model to derive modeled measurements, comparing these to the true measurements, and running these measurement residuals (weighted using assumed measurement error statistics) backwards in time through the adjoint of the transport model to obtain flux corrections, then repeating. The flux inversion is posed mathematically as a minimization problem, with the adjoint run providing the gradient to the measurement portion of the cost function. We use the 2nd-order Broyden-Fletcher-Goldfarb-Shanno (BFGS) method to solve for the flux estimates, obtaining a low-rank covariance matrix for errors in the flux estimate.

2.4 Simulation approach

The assimilation seeks to drive an initial (a priori) guess of the fluxes towards the real-world ("true") fluxes, using the measurements. In our simulations here, we generate measurements with different error sources added on that attempt to describe the real errors OCO will encounter when it actually flies, then process the measurements with the assimilation method in the same way that we would do with the real data. Since we know the fluxes used in generating the data, we can compare the estimated fluxes to these "true" values to get actual estimation errors. If only random estimation errors are added to the data in a perfect-model setup (see Experiments 1 and 2, Sect. 2.6), the statistics of these estimation errors should be consistent with what would be given by the full-rank covariance matrix, if one were computed. To approximate the uncertainties that would be given by the covariance matrix, we compile our random estimation error

statistics over seasons (13 weekly flux values) and over a full year (52 values, as done in Chevallier et al., 2007a).

Our simulation approach has the added benefit of allowing us to quantify the impact of systematic errors, such as measurement biases or errors in the transport model, with the same statistics as for the random error experiments. In the first case, the biases are added when simulating the true measurements; in the second case, different winds are used in the optimization than are used to generate the truth.

For our true fluxes, we use monthly land biospheric fluxes from the LPJ model (Sitch et al., 2003) and monthly ocean fluxes from a biospheric run of the NCAR ocean model (Doney et al., 2004; Najjar et al., 2007); both are then interpolate to daily values. For our a priori fluxes, we use similar fluxes from the CASA land biosphere model (Randerson et al., 1997) and the Takahashi et al. (1999) ocean CO_2 flux product. Figure 2a–c gives snapshots of both sets of fluxes for January and July, as well as their difference. While both sets of fluxes show similar features (e.g., the seasonal cycle of net photosynthesis minus respiration in both the northern and tropical land vegetation, uptake of CO_2 by the extra-tropical oceans versus outgassing by the tropical oceans), their timing and spatial details vary enough that the prior-truth difference (Fig. 2c) is often as large as the fluxes from either model. Thus, the OCO data hold much promise for improving the models, even if the models appear to be doing a fair job of describing the basic biogeochemical processes at the moment.

The prior-truth flux differences (Fig. 2c) show systematic spatial and temporal correlations. The spatial correlations are often at fine scales, many times associated with deserts and mountain ranges: thin lines of ± values running parallel to the Canadian Rockies, for example. Because of the physical basis of these differences, we have some hope that the differences between our two sets of models will bear some resemblance to the difference between any one model and the real-world fluxes. The Bayesian prior in our cost function performs the useful function of damping out spurious noise in the estimate due to noise in the measurements (or model-measurement mismatches). However, inaccuracies in our knowledge of the a priori flux error covari-

ACPD
8, 20051–20112, 2008

ance, $\mathbf{P}_o$, including both correlations and the overall magnitude of the variances, will impact the final assimilated estimate, both the value of the estimate itself as well as how rapidly the assimilation converges to it. We use the absolute value of the actual prior-truth flux difference (Fig. 2d) in $\mathbf{P}_o$ for most of our assimilation experiments (see Sect. 2.6), but also use an imprecise estimate (Fig. 2e) in a sensitivity experiment to examine the impact of realistic errors in the assumed $\mathbf{P}_o$.

We have not included fossil fuel fluxes in these simulations: errors in our best estimate of the fossil fuel source are thought to be small at our $2^{\circ}\times5^{\circ}$ resolution. The net flux uncertainties we obtain over land should thus be thought of as applying to the sum of the fossil and land biospheric fluxes. Similarly, the diurnal cycle of flux is not modeled here, since the OCO data, taken at a single local time per day, cannot resolve it.

2.5 X_{CO_2} measurement errors and averaging kernels

The assimilation requires a statistical description of the errors in individual X_{CO_2} measurement retrievals, as well as knowledge of the averaging kernel (AK – how strongly each vertical layer contributes to the column average). Past simulation studies of this sort (Baker et al., 2006b; Chevallier et al., 2007a) have used simplified assumptions for both quantities: flat mass-weighted averages in the vertical, as well as measurement errors of 1 or 2 ppm, with only a single measurement being used in each separate grid box. Bösch et al. (2008) have obtained new estimates of both quantities as a function of surface type, SZA, aerosol OD, and pointing mode (nadir vs. glint) (Fig. 3). They used a detailed radiative transfer scheme to simulate the radiances seen in the measured OCO spectral bands, then fed these through the OCO "full-physics" X_{CO_2} retrieval scheme, testing sensitivities to various error sources. We use these improved error and AK estimates, along with surface FOV locations and SZAs taken from an accurate OCO orbit generator for both nadir and glint pointing modes, to calculate realistic values single-sounding X_{CO_2} retrieval errors and AKs around the orbit.

There are potentially hundreds of separate measurements (with FOV areas up to

2.7 km^2) along the ~10 km-wide FOV ground track swath crossing any of our 2°×5° atmospheric model grid boxes. Since these measurements are taken over an often heterogeneous surface with different reflective properties and CO_2 emissions, with varying cloud and aerosol amounts interfering with the retrieval, the measurement errors along the swath could be quite variable. When averaged across the grid box, the uncorrelated portion of these errors could be expected to cancel out significantly. We make an attempt here to estimate what portion of this error cancels out and what does not, to quantify the effective measurement error of all the valid retrievals inside each 2°×5° model grid box. In computing this effective error, we consider the probability of obtaining cloud-free retrievals with aerosol ODs lower than a 0.30 cutoff, and we model correlations along the orbit as a function of SZA. The along-orbit computation of the AKs and single- and multi-sounding retrieval uncertainties are done first at a 1°×1° resolution, then translated to the 2°×5° model grid box resolution based on the time spent in each 1°×1° area inside the 2°×5° box. We show annual mean plots here for the uncertainties and quantities used to compute them, but they vary monthly in the simulations (see the Supplementary Material for seasonal plots http://www.atmos-chem-phys-discuss.net/8/20051/2008/acpd-8-20051-2008-supplement.pdf).

Again, we go beyond the previous studies in representing the X_{CO_2} retrievals in two ways: 1) we use the more accurate single-sounding X_{CO_2} retrieval errors and averaging kernels obtained by Bösch et al. (2008), and 2) we factor in the combined information available from all retrievals across each 2°×5° model grid box to compute a lower "effective" X_{CO_2} retrieval error for use in the flux assimilations.

2.5.1 Single-sounding X_{CO_2} errors and supporting fields

The calculation of the SZA and the FOV location on the surface, required for the X_{CO_2} error and AK calculations, both depend on an accurate orbit propagation. For nadir mode, the FOV is located at the sub-satellite point. For glint mode, the surface normal at the glint spot is computed by iteration until the surface normal is the same

angle from the sun and the satellite position vectors, in the plane they define. In both pointing modes, the surface normal is computed assuming the Earth is an oblate spheroid. The orbit is taken as sun synchronous, with a 13:18 local time ascending node, a=7083.45 km, e=0.0012, i=98.2°. The anomaly is chosen arbitrarily to have the spacecraft crossing north across the equator at 00:00:00 on 1 January.

We compute monthly values of SZA and aerosol OD, as well as a constant surface cover type, on the 1°×1° grid. From these, the X_{CO_2} retrieval errors and AKs from Bösch et al. (2008), may be mapped out as a function of position around the globe. These 1°×1° maps are then sampled as a function of position around the OCO orbit to obtain detailed X_{CO_2} retrieval errors and AKs for use in the assimilation. Figure 4a gives the distribution of the five surface types used to calculate the X_{CO_2} errors and AKs: ocean/water, snow/ice, desert, conifer (representing all types of dense vegetation), and sparse vegetation/exposed soil. Figure 4b gives median total aerosol ODs derived from Aqua/MODIS data. The aerosol OD histograms used to compute these medians are described in more detail in Bösch et al. (2008). Computed solar zenith angles as a function of latitude for four seasons are given in Fig. 5a. Finally, the OCO single-sounding X_{CO_2} retrieval uncertainties calculated from these fields are given in Fig. 6a for both nadir and glint pointing modes. The most striking feature of Fig. 6a is how much lower the uncertainties are over the oceans in glint mode as compared to nadir mode. Note also, however, that they are somewhat lower over the land in nadir mode compared to glint.

2.5.2 Computing effective multi-sounding X_{CO_2} errors at the 1°×1° resolution

Our ability to represent the OCO X_{CO_2} retrievals is limited by the fairly coarse spatial resolution of our transport model: a transport model with grid boxes ~220 km wide cannot represent the X_{CO_2} variability occurring in the real world at shorter spatial scales. However, for the purposes of estimating CO_2 concentrations and fluxes at scales of 100s to 1000s of km, there is no need to model every ~2.7 km^2 X_{CO_2} retrieval correctly. The real question is this: how close does the average of all the X_{CO_2} measurements

ACPD
8, 20051–20112, 2008

taken inside a model-scale grid box come to the average of all true X_{CO_2} values across the full area of that grid box (not just inside the ~10 km-wide OCO FOV track)? The model could describe the full-grid-box average X_{CO_2} correctly.

The first point to note is that even if the X_{CO_2} measurements are perfect and complete (no data gaps due to clouds or aerosols) across the full length of the 10 km-wide FOV ground track, there will still be a difference between this perfect ground track average and the average X_{CO_2} across the full grid box. Second, the perfect X_{CO_2} measurements may not even get the ground track average correct, because of non-uniform coverage (data gaps) due to clouds and aerosols. And, third, the X_{CO_2} measurements are obviously not perfect, but are subject to the measurement errors discussed above. When all the X_{CO_2} measurements inside a grid box are averaged together, their errors may cancel out to some extent in the average, but there will still be a remaining error between the average measurement and the true X_{CO_2} value for the measured portion of the ground track. All three of these errors – track-to-box representation error, along-track representation error, and average effective measurement error – must be combined to get the model-measurement mismatch error that should be fed into the flux error simulations.

The first two of these error sources have been examined by Corbin et al. (2008). They did detailed simulations of X_{CO_2} variability inside domains of 1°×1° and 4°×4° using a mesoscale atmospheric transport model, comparing the X_{CO_2} averages along an OCO-like FOV ground track to the average values across the full domain to obtain estimates of the track-to-box representation errors. They also simulated the effect of clouds on the availability of OCO retrievals, coming up with realistic estimates of the along-track representation errors. For the two sites they examined, they concluded that the along-track representation error was small compared to the track-to-box representation error. They also concluded that the track-to-box error was, in turn, largely random and relatively small compared to the measurement errors. In our study here, we neglect the along-track errors, and extrapolate the Corbin et al. (2008), track-to-box representation errors from their two sites to the full globe using a fit proportional to

ACPD
8, 20051–20112, 2008

the absolute value of the net ocean or land biosphere flux from our monthly-varying a priori flux model inside each 1°×1° grid box (Fig. 6c, with a proportionality factor of 2.5×10^6 ppm/kg CO_2 m^{-2} s^{-1}). These track-to-box representation errors are taken to be unbiased and gaussian, and are added in all the simulation cases presented here.

The third error source, the effective joint error of all the individual X_{CO_2} measurements inside a grid box, is the largest over almost all of the globe at all times of the year. To compute it, one must factor in data gaps due to cloud coverage or aerosol ODs greater than 0.30 (the level beyond which the OCO retrievals will not be routinely performed). Furthermore, one must estimate the error correlation along the ground track of near-by measurements. Here we assume that errors from aerosols and clouds will dominate the correlated errors (both directly by causing single-sounding retrieval biases that are correlated along-track, and indirectly by introducing data gaps of finite extent that cause representation errors) and that their correlation lengths increase with SZA and path in atmosphere. We represent this with a simple ad hoc correlation length L:

$$L^2 = (c_w^2 + (P * c_h * \tan(\mathrm{SZA}))^2) \quad (1)$$

where c_w is a fine-scale cloud width (taken here as 4 km), c_h is a typical average cloud height (taken here as 7 km), and P is a path-length factor (taken as 1 for nadir pointing mode and 2 for glint). The maximum number of possible independent measurements inside a 1°x1° grid box is then taken to be $N_{\max}=p_{1°\times1°}/L$, where $p_{1°\times1°}$ is the OCO FOV ground track path length inside the box. This maximum value is reduced by the availability of data due to clouds and aerosols, giving N_{eff}, the effective number of independent X_{CO_2} measurements inside the 1°×1° grid box, as

$$N_{\mathrm{eff}} = p_{1°\times1°}/L * P_{\mathrm{cloud-free}} * (1 - P_{\mathrm{HiAeroOD}}) \quad (2)$$

where P_{HiAeroOD} is the probability of aerosol ODs exceeding the 0.30 value beyond which OCO X_{CO_2} retrievals are not attempted, and $P_{\mathrm{cloud-free}}$ is the probability of finding at least one cloud-free scene in a swath of OCO FOV ground track of length L. P_{HiAeroOD}

is computed from the same aerosol OD histograms as the median aerosol ODs, from Bösch et al. (2008). $P_{\text{cloud-free}}$ is computed from climatologies of Aqua/MODIS and Terra/MODIS data, sampled in 10 km-wide swaths, as detailed in the Appendix.

Both aerosol and cloud coverage are calculated using data from the MODIS instrument aboard NASA's Aqua satellite, which flies in the same "A-train" orbit as OCO will. MODIS has a 1×1 km FOV that, being close to the ~2.7 km^2 OCO FOV area, should give realistic idea of cloud free areas and aerosol amounts over most areas. Since the MODIS instrument scans up to 45° off-nadir, the sensed radiation actually passes though a slightly longer path than that for OCO in nadir mode, encountering if anything more clouds and aerosols. For OCO in glint mode, however, the path length of the radiation in the atmosphere can be quite a bit longer than that sensed by MODIS. To account for the increased probability of encountering clouds and aerosols at SZAs greater than 20° in glint mode, we use these adjusted formulae:

$$P_{\text{cloud-free}} = P_{\text{cloud-free\_MODIS}}^{(2/(1+\cos(\text{SZA})/\cos(20^\circ)))} \quad (3)$$

P_{HiAeroOD} is recomputed by shifting the 0.30 OD cutoff to a lower value of 0.30* (2/(1+cos(SZA)/cos(20°))) and summing aerosol OD histogram to the right of this new value. Once N_{eff} is calculated, the effective measurement error accounting for all X_{CO_2} measurements inside each 1°×1° grid box, is given as: $\sigma_{\text{eff},1\times1}=\sigma_{1\text{shot}}/\sqrt{N_{\text{eff}}}$.

The effective measurement uncertainties at 2°×5° resolution used in the assimilation are then computed from these 1°×1° values, based on the distance $I_{1\times1}$ and $I_{2\times5}$ inside each 1°×1° and 2°×5° box, as: $I_{2\times5}/\sigma^2_{\text{eff},2\times5}=\sum_i I_{1\times1,i}/\sigma^2_{\text{eff},1\times1,i}$.

Figure 6b gives the distribution of $\sigma_{\text{eff},1\times1}$ and Fig. 7, N_{eff}, along with the $P_{\text{cloud-free}}$ and P_{HiAeroOD} values used to compute them. Figure 7b, c shows that both persistent cloudiness and areas of high aerosol contamination significantly reduce the availability of OCO measurements in this approach. The $\sigma_{\text{eff},1\times1}$ values in Fig. 6b are substantially higher than the track-to-box representation errors given in Fig. 6c, by generally more than a factor of 5. The areas of low error in both Fig. 6b and 6c show where the measurements with the greatest information content will occur; the assimilation convolutes

ACPD
8, 20051–20112, 2008

these with transport to determine where the flux constraints will be the strongest.

2.6 Flux estimation simulations

The main objective of our study is to perform a series of OSSEs meant to represent how well our data assimilation system will estimate surface CO_2 fluxes, given the presence of various error sources. We somewhat arbitrarily divide these errors into purely random ones (modeled as unbiased, gaussian noise) and biases constant in space and time. In reality, of course, there is a spectrum of errors that are correlated in both space and time that fall between these extremes, due to correlations in such error-causing factors as scattering due to aerosols and undetected clouds, spectral effects, and surface reflectance properties. We have attempted to account for some of these terms above by transforming the correlated errors into the corresponding purely random problem using the idea of "effective independent measurements". Since the finest-resolution unit the atmospheric transport model, and thus the atmospheric flux assimilation, can deal with is the transport model grid box at the model time step, both random and systematic errors are quantified at that scale: what is the net bias or random error between the weighted average of all measurements in a grid box (in a single orbit) and the true concentration in that box?

Table 1 outlines a series of assimilations we perform, with the error sources that have been added in each case. Two of the sources of error described above – the "track-to-box" representation errors and the random measurement errors – have been added in all the experiments as gaussian noise. Biases due the representation errors were found to be small in Corbin et al. (2008) and are not added here at all. Systematic errors in the measurements have been added onto to true measurements in Experiments 4–6 (Table 1) described below. Whenever these systematic errors are added, we increase the assumed random measurement uncertainties in an attempt to account for them. Although it is not formally statistically valid to represent systematic errors with random ones, it is often done and is certainly better than not attempting to account for the biases, since in that case the measurements would be given too much weight vis-

ACPD
8, 20051–20112, 2008

a-vis the prior and the impact of the biases would be greater than if the measurements had been de-weighted (Chevallier, 2007c). In all experiments, both the measurement error and a priori flux error covariance matrices, **R** and $\mathbf{P}_o$, are diagonal: we account for correlations in the measurements by computing the effective number of independent measurements and adjusting the multi-sounding measurement uncertainties accordingly, and we neglect both time and space correlations between the estimated weekly fluxes at a $1^\circ \times 1^\circ$ resolution.

Experiments 1 and 2 can be thought of as "perfect model" experiments for nadir and glint mode data. There is no transport error: the same model that was used to generate the true data is used in the assimilation. There are no measurement biases added, only random measurement errors. And the assimilation is perfectly "tuned": both the assumed measurement error covariance matrix and the assumed a priori flux estimation error covariance matrix are chosen to be consistent with the statistics of the added measurement errors and of the model-truth flux errors, respectively. With these assumptions, the flux errors that result from the assimilation should agree with the error statistics that would be given by the a posteriori flux covariance matrix of inverse methods that produce one (our assimilation here does not produce a full rank covariance matrix, only a low-rank approximation not useful for quantitative error analyses at the fine scales examined here). Such a posteriori covariance matrices are often the end product of error analyses and are useful for quantifying the precision of the assimilation (though not necessarily the accuracy, since they do not quantify the impact of systematic errors). The variances in the a priori flux error covariance matrix were taken to be the square of the actual prior-truth flux difference given in Fig. 2c.

The remainder of the tests were done only for glint viewing mode. In Experiment 3, we add more realism by "mistuning" the assimilation, adding realistic errors to both the assumed a priori flux error and measurement error covariance matrices. Instead of making the a priori flux uncertainties proportional to the actual prior-truth flux difference (Fig. 2d), we use uncertainties based only on our a priori flux patterns (Fig. 2e, since, in real world simulations, we have no knowledge of the true fluxes or their errors). To

ACPD
8, 20051–20112, 2008

mistune the assumed measurement error covariance matrix **R**, we actually change the added measurement uncertainties from the glint mode values in Fig. 6b to those shown in Fig. 6d; we keep the assumed values the same as in the other experiments to allow the cost function values to be compared with the other experiments more readily. To obtain the values in Fig. 6d, we simplified the SZA-dependent glint mode X_{CO_2} retrieval errors (Fig. 3a) as follows: for the conifer and sparse vegetation surface types, the measurement errors were taken to be 0.60 and 0.50 ppm, respectively, for SZAs under 55°, and 0.70 and 0.90 ppm over 55°; over deserts and snow, 0.40 and 1.10 ppm under 45°, and 0.75 and 3.00 ppm over 45°; and over water, 0.40 ppm for all SZAs.

If only random errors were present in our estimation problem, the results of Experiment 3 might give a realistic view of the estimation errors we should expect using the real OCO measurements. Unfortunately, those results will also be corrupted by a range of systematic errors. In Experiment 4, we examine one source of these: measurement biases, taken here as seasonally-varying and proportional to the median aerosol ODs (*aero_OD*) summarized in Fig. 4b. Biases due to aerosols are expected to cause the main systematic errors in the OCO X_{CO_2} retrievals (Connor et al., 2008). Over land and ice-covered areas, a bias of $+\alpha$**aero_OD* is added to all measurements, while over the ocean, a bias of $-\alpha$**aero_OD* is added. The proportionality constant α=1 ppm/OD; the maximum bias is ±0.3 ppm (no X_{CO_2} retrievals being attempted for aerosol ODs greater than 0.3). We have also performed Experiment 4b in which twice these aerosol biases were added (α=2 ppm/OD up to a maximum of 0.6 ppm). The magnitude of the biases added in these two experiments range from being comparable to the multi-sounding random measurement uncertainties (1σ) over land in the first case, and twice that in the second case. To account for this extra error in the assimilation, we add the aerosol bias uncertainties given in Fig. 6e to the assumed multi-sounding random measurement uncertainties (Fig. 6b and 6c) in quadrature; these are doubled for Experiment 4b. (The values added to the assumed errors (Fig. 6e) are actually twice as high as the added biases to account for two effects: the assumed errors at 1°×1° in Fig. 6e will drop by a factor of $\sqrt{2}$ when averaged across the 2°-wide grid boxes on

ACPD
8, 20051–20112, 2008

which scale the biases are added, and 50% of the area under a gaussian curve falls withing $\pm 0.676\sigma$, requiring a larger 1σ value to represent a bias; $\sqrt{2}/0.676 = 2.09 \approx 2$)

Measurement errors are not the only systematic errors affecting the flux assimilation: the atmospheric transport models used to relate concentrations to fluxes have a variety of errors, not only in their representation of the broad-scale general circulation, but also in their smaller-scale mixing processes (especially between the planetary boundary layer and the free atmosphere). In Experiment 5 we add a version of these instead of the measurement biases. As a simple approximation of these errors, the winds and other mixing parameters that drive the transport model are shifted forward by 17 h in generating the truth as compared to those used in the assimilation. This captures errors in both the synoptic meteorology as well as in the timing of the diurnal cycle of mixing. At the same time, we add the transport uncertainties in Fig. 6f to the assumed measurement uncertainties to account for the transport errors; these are taken as the mean of the absolute values of the true and prior fluxes (Fig. 2a, b), divided by the factor 4.0×10^{-7} kg CO_2 m^{-2} s^{-1} ppm^{-1} between latitudes $\pm 29^{\circ}$ and 2.0×10^{-7} kg CO_2 m^{-2} s^{-1} ppm^{-1} outside that. This ad hoc estimate is based on the idea that the largest transport errors occur where the surface flux variability is the greatest, and that this occurs where the fluxes themselves are the greatest. The factor of two difference between the tropics and extra-tropics is meant to account for the greater prevalence of horizontal motions in the extra-tropics that are likely to cause spatial mis-attribution of the fluxes.

Finally, we examine the combined effect of the transport errors from Experiment 5 and the aerosol biases of Experiments 4 and 4b in Experiments 6 and 6b.

3 Results

The goal of our data assimilation approach is to use concentration measurements to drive an a priori flux estimate towards the true fluxes. We will examine the root mean square (RMS) estimate-truth differences (or "errors") in both the 7-day fluxes

ACPD
8, 20051–20112, 2008

directly estimated by the assimilation, as well as in the seasonal fluxes they imply. (Annual-term mean fluxes would be of more interest for climate research, but since we have only examined a single year we cannot calculate robust error statistics for them; our seasonal mean statistics should be similar to the annual mean ones, we feel.) We make heavy use of the fractional error reduction statistic, given by (RMS_{prior}–RMS_{post})/RMS_{prior}, since it more clearly distinguishes areas of small versus large improvement. Finally, we only discuss the RMS errors accumulated across the full annual cycle here; for a seasonal breakdown, see the Supplementary Material http://www.atmos-chem-phys-discuss.net/8/20051/2008/acpd-8-20051-2008-supplement.pdf.

3.1 Perfect-model simulations

A posteriori RMS 7-day flux error reductions obtained using data from nadir- and glint-mode OCO observations (Experiments 1 and 2) after several different descent iteration counts of the assimilation algorithm are presented in Fig. 8. (For a direct comparison of the a priori and a posteriori flux errors, see Fig. S4 in the Supplementary Material http://www.atmos-chem-phys-discuss.net/8/20051/2008/acpd-8-20051-2008-supplement.pdf.) The nadir observations provide little improvement over the oceans (not surprising, given the very high measurement errors there) but impressive improvements over the land – on the order of 45% in most areas, especially where the initial flux errors (Fig. 2c, d) are largest. The glint mode improvement over land is similar in magnitude to that of nadir mode – surprisingly, given that the effective glint mode measurement uncertainties are larger over land than the nadir ones (Fig. 6b). Apparently, enough land flux information blows out over the ocean for the more precise glint mode measurements there to compensate for the less precise and/or less available glint mode measurements over the adjacent land regions. As might be expected, the ocean flux improvement in glint mode is much better than in nadir; in fractional terms, it is as large as the improvement over the land, over 45% in the areas where the initial errors are the largest. Since glint mode measurements give lower flux errors over a broader area than nadir mode (and do equally as well over the

land), we focus on glint mode in the remaining experiments.

Since improvements are less impressive in the areas with low initial flux errors, it appears that the assimilation corrects the largest flux errors during the initial descent steps of the optimization, moving to the finer-scale corrections only later. This flux convergence behavior can be seen in Fig. 9b and 9c, which give the global flux convergence in terms of both flux errors weighted as in the cost function (i.e., the error sum that the assimilation seeks to minimize) and the absolute (un-weighted) errors that the eye would see on a flux graph. In terms of both error measures, errors over the land regions are removed first, with the initially-lower errors over the oceans being reduced only later. After iteration 30, in fact, the land flux errors actually grow again in both measures, while the weighted ocean and land+ocean errors both decrease. Since the lower-flux areas (such as the oceans) were not fully converged after 50 iterations in glint mode, we ran both perfect model cases out to 100 iterations. Figure 8 shows how the ocean errors gradually decrease as the optimization continues, at the cost of higher absolute errors over land. The tradeoff between land and ocean errors occurs for both nadir and glint modes in these perfect model simulations.

Figure 9c shows that nadir mode measurements actually give lower absolute (un-weighted) flux errors than glint mode after converging about 25 descent steps – the most converged point on the convergence trajectory for absolute land flux errors as well as absolute land+ocean errors – before the land errors increase again as the assimilation converges smaller absolute flux errors, mostly over the oceans. If we did not care about optimizing fluxes over the ocean, and if we had some way of knowing at which iteration this land minimum was reached in a real assimilation, then we could just stop the assimilation there and achieve the large fractional reductions over land given in Fig. 8c. As Fig. 9c shows, something similar happens with glint mode measurements, though the nadir mode measurements give lower errors overall at the minimum. In an assimilation with real data (in which the truth is not known) it would not be possible to make flux convergence plots like this to know at which iteration the minimum is reached. One could, however, achieve these somewhat lower land errors by forgoing

ACPD

8, 20051–20112, 2008

any improvement over the oceans by setting the a priori flux uncertainties over the ocean to unrealistically low values; the ocean flux values would change little from the a priori values in that case, most of the work done by the assimilation would go towards improving the land fluxes, and there would be only a small rebound in the land errors after the minimum.

The a posteriori error statistics given by these perfect model experiments correspond to those from a single draw from the a posteriori estimation error covariance matrix, if our method were to compute one. While they do not include systematic errors, they provide a useful "best case" error estimate – if the measurements are not precise enough to meet their design goals in this view, they never will be when all the other systematic error sources are added in. We address these other errors next.

3.2 Estimation errors with a "mistuned" assimilation

When the measurement noise and a priori flux error covariance matrices assumed in the assimilation ($\mathbf{R}_a$ and $\mathbf{P}_{o,a}$) are not equal to those corresponding to the true measurement noise added ($\mathbf{R}_t$) and the true statistics of the prior-truth flux fields ($\mathbf{P}_{o,t}$), then we call the assimilation "mistuned". For a basic Bayesian cost function

$$J=(\mathbf{H}\boldsymbol{x}-\boldsymbol{z})^T\mathbf{R}_a^{-1}(\mathbf{H}\boldsymbol{x}-\boldsymbol{z})+(\boldsymbol{x}-\boldsymbol{x}_o)^T\mathbf{P}_{o,a}^{-1}(\boldsymbol{x}-\boldsymbol{x}_o),$$

where $\boldsymbol{x}$ and $\boldsymbol{x}_o$ represent the estimated and a priori state vector, $\boldsymbol{z}$ the measurements, and $\mathbf{H}$ the measurement matrix, the true a posteriori covariance matrix in that case is given by

$$\mathbf{P}_x = [\mathbf{H}^T\mathbf{R}_a^{-1}\mathbf{H}+\mathbf{P}_{o,a}^{-1}]^{-1}[\mathbf{H}^T\mathbf{R}_a^{-1}\mathbf{R}_t\mathbf{R}_a^{-1}\mathbf{H}+\mathbf{P}_{o,a}^{-1}\mathbf{P}_{o,t}\mathbf{P}_{o,a}^{-1}][\mathbf{H}^T\mathbf{R}_a^{-1}\mathbf{H}+\mathbf{P}_{o,a}^{-1}]^{-1} \quad (4)$$

and no longer reduces to the simplified form $\mathbf{P}_x=[\mathbf{H}^T\mathbf{R}_a^{-1}\mathbf{H}+\mathbf{P}_{o,a}^{-1}]^{-1}=\mathbf{P}_{x,a}$. To produce a posteriori error statistics corresponding to what would be given by a full-rank covariance matrix with our simulation setup, we had to impose perfect agreement between the assumed errors statistics for the measurement noise and the prior flux errors. We set $\mathbf{R}_t=\mathbf{R}_a$ by adding measurement noise to the data using the using the statistics from

$\mathbf{R}_a$, and we chose $\mathbf{P}_{o,a}$ to agree with the actual (known) prior-truth flux difference. This was done in the perfect model case discussed above (Exps. 1 and 2). However, in a real-world assimilation, one has only an imprecise idea of what $\mathbf{R}_t$ and $\mathbf{P}_{o,t}$ should be, so $\mathbf{R}_a \neq \mathbf{R}_t$ and $\mathbf{P}_{o.a} \neq \mathbf{P}_{o,t}$ and the covariance from Eq. (4) applies; this is captured in our error statistics when we mistune $\mathbf{P}_{o,a}$ and $\mathbf{R}_a$.

The most noticeable effect of the mistuning of both $\mathbf{P}_{o,a}$ and $\mathbf{R}_a$ (Experiment 3), as seen in Fig. 9, is a slowing of the convergence of the descent algorithm. (We have done a separate assimilation, not shown here, that verifies that this slowing is due almost entirely to the mistuning of $\mathbf{P}_{o,a}$, rather than $\mathbf{R}_a$.) This slowing of the convergence makes sense. The a posteriori fluxes in our assimilation are found using the 2nd order BFGS minimization approach. If one were to know the exact a posteriori covariance matrix $\mathbf{P}_x$ at the start, this technique would converge to the optimal estimate in a single step from any prior guess. Of course, $\mathbf{P}_x$ is not known beforehand, but a good guess of $\mathbf{P}_o$, used in setting the starting value of the Hessian matrix, can precondition the search and speed convergence. When $\mathbf{P}_{o,a} \neq \mathbf{P}_{o,t}$, then $\mathbf{P}_{o,a}$ is a poorer approximation of the prior portion of Eq. (4), $\mathbf{P}_{x,a}\ [\mathbf{P}_{o,a}^{-1}\mathbf{P}_{o,t}\mathbf{P}_{o,a}^{-1}]\ \mathbf{P}_{x,a}$, and thus the minimization is preconditioned worse and takes longer to converge. Put another way, the fine scale spatial detail about the prior-truth difference that one knows if $\mathbf{P}_{o,a}=\mathbf{P}_{o,t}$ is a great help in converging to the truth, but of course would never be known in a real situation.

Because of this slower convergence, we must run the mistuned case (Exp. 3) out many more iterations to get to the same point on the convergence trajectory as in the perfect model case (Exp. 2). After 130 iterations, the 7-day flux results would seem to have convergence to the equivalent of somewhere between iterations 25 and 40 from Experiment 2 (Fig. 8), with perhaps a 10% degradation of the flux improvements (e.g., from 50% to 40%). Probably of greater importance than this error degradation, however, is the slowing of the convergence rate, especially if this causes runs to be truncated due to computational cost before adequate convergence is achieved. Because this degradation in the improvement is relatively small compared to that due to the other systematic errors addressed below, to speed the convergence for the re-

ACPD
8, 20051–20112, 2008

mainder of our experiments we will reset $\mathbf{P}_{o,a}$=$\mathbf{P}_{o,t}$ and $\mathbf{R}_a$=$\mathbf{R}_t$ and assume that the mistuning errors at a similar point in the convergence trajectory can be added back on after the fact.

For the remaining systematic error experiments, we plot the 7-day and seasonal flux error reductions (Figs. 10 and 11) after 50 descent steps of the assimilation method using glint mode data only. Note that the seasonal mean flux improvements (Fig. 11; RMS of four 13-week spans) are generally similar to the 7-day values (Fig. 10) over the ocean, but significantly higher over the land. For the perfect model case, the initial errors are reduced by over 45% almost everywhere over land, and in many areas where the initial errors were largest, by over 65%.

3.3 The impact of aerosol-related measurement biases

Adding a bias proportional to aerosol depth, while compensating for it by increasing the measurement uncertainty (Experiment 4), causes a small degradation in the assimilated 7-day fluxes over land (compare Fig. 10c to 10a; Fig. 9c), most noticeably around the edges of the continents and around the high aerosol regions of equatorial Africa, the Sahara, and India. Over the oceans, the impact is larger, especially in the North Pacific and across the extra-tropical southern oceans. The impact of the biases is more noticeable for the seasonal fluxes (Fig. 11), especially over the land, where most of the flux improvements that were over 75% in the unbiased case are degraded to below that when the aerosol biases are added.

When these aerosol biases are doubled (Experiment 4b, Figs. 10d, 11d), the degradation is amplified and again the worst effects are over the oceans. The degradation of the seasonal fluxes appears worse than for the 7-day fluxes, perhaps because there is more improvement to lose there. Even so, there are still large areas where improvements over 65% remain in the seasonal flux error reductions, particularly in the interior of the continents.

ACPD
8, 20051–20112, 2008

3.4 Impact of transport errors

The 17 h shift in winds added in Experiment 5 has the largest impact on the estimated fluxes over the extra-tropics (compare Fig. 10b to 10a), especially over North America and east Asia where the jets are the strongest. The near-surface winds in the extra-tropics are predominantly horizontal, so transport errors there lead to horizontal errors in where the flux corrections are placed. Over the tropics, however, wind motions are more vertical, due to the weak Coriolis force and the dominance of convection; transport errors affect more where concentrations are distributed in the column (having little impact on the column-integrated measurement) and less the horizontal assignment of the fluxes. Despite this argument, there also seems to be a sizable degradation in the flux estimates over the tropical Pacific Ocean, perhaps reflecting the importance of the trade winds there.

Compared to the aerosol bias impact, the effect of transport error on the 7-day flux estimates is similar in the tropics, not as bad over the northern oceans, and worse over the extra-tropical continents, especially over North America and parts of Eurasia, leading to larger global flux errors than in either aerosol bias experiment (Fig. 9c). The impact on the seasonal flux error reductions (Fig. 11), however, is different: the transport errors generally have a smaller impact than the aerosol bias errors everywhere, except over North America and some ocean areas, where they are similar. Unlike the aerosol biases, which vary slowly across the year, the transport errors are more variable and their effect on the inverted fluxes cancels out to a large degree when averaged over longer spans.

3.5 Impact of both aerosol-related measurement biases and transport errors

When the effects of both transport and measurement bias errors (Exps. 6, 6b) are compared with the effects of either one of the systematic errors (Exps. 4, 4b, and 5) at iteration 50 in all cases (Figs. 10 and 11 for weekly/seasonal), the flux improvements are degraded more than for either error source by itself. In terms of the seasonal error

ACPD
8, 20051–20112, 2008

reductions (Fig. 11e, f), there are still broad areas over land with improvements of 50% or higher, even in the doubled aerosol bias case. Error reductions over the oceans are less encouraging, most areas being under 15%. Improvements in the 7-day fluxes are 10–20% lower over the land and similarly low over the ocean. Since the remaining improvement seen in Figs. 10f and 11f were obtained in perfectly-tuned experiments, they must be decreased further by the mistuning effects seen in Fig. 8b to include the effects of all error sources examined here.

There are a few areas where the improvements in Experiment 6 were actually greater than in the individual error source experiments (4 and 5), areas where in Experiments 4 and 5 the assimilation led to results that were actually worse than the prior. This may reflect mis-tuning of the assumed errors in those experiments: in particular, the additional error added to the assumed measurement uncertainty to account for the transport errors (Fig. 6f) may not be large enough or may not have the proper spatial pattern. Errors like this made in incorrectly increasing the measurement uncertainties to account for systematic errors represent another "mistuning" in the assimilation.

3.6 Impact of systmatic errors at coarser scales

For climate research, flux averages over annual scales (and longer) are of more interest than the weekly and seasonal fluxes discussed above. Figure 12 gives the annual mean (a posteriori-true) flux errors for the different error experiments. The corresponding fractional error reductions (not shown) are noisy – there is only a single term in the required RMS error sums, because only a single year of data was simulated here, so random errors do not cancel out – but, where positive, are generally larger than the seasonal error reductions in Fig. 11. This suggests that the more statistically significant fractional reductions we obtain for the seasonal flux errors (Fig. 11) may be a good proxy for the annual mean error reductions across the full globe. It was not clear that this would be the case before doing these tests: the magnitude of the a priori errors in the seasonal fluxes is generally higher than in the annual means, especially over land, and since these magnitudes are in the denominator of the error reductions, one might

ACPD
8, 20051–20112, 2008

think that the seasonal error reductions would be higher.

The annual mean errors from the perfect model runs (Fig. 12) are characterized by alternating regions of counterbalancing errors over the global land areas, with scales of ~1000–2000 km. The ocean errors vary across longer scales but are weaker. For the experiments with systematic errors added, the errors grow and take on coarser scale patterns over the land regions. Much of the alternating ±errors over land should cancel out when integrated over larger regions. In Fig. 13, we integrate the seasonal and annual mean flux errors across the 22 globe-spanning regions from the Transcom3 (T3) flux inversion intercomparison project (see Fig. 1 from Baker et al., 2006a for a map). The RMS seasonal errors (plotted as negative values) for the 11 land regions drop from a priori values of ~0.5–2.0 PgC/year to ~0.1–0.2 PgC/year for the perfect model experiments. When the transport and aerosol bias errors are added on, these land errors increase to ~0.3 PgC/year, still low enough to give a great improvement over the a priori estimates. For the annual mean errors (absolute values plotted in the positive direction) over land, a priori errors in the range of ~0.1 to 0.5 PgC/year are reduced to generally below 0.1 PgC/year in the perfect model experiments, but rise back up to 0.1–0.2 PgC/yr when the systematic errors are considered. For those T3 regions with the largest initial errors, the errors are halved at least, while those with the smallest initial errors see little to no improvement. Over the oceans, where the seasonal cycles are less pronounced, error reductions of up to 50% are obtained for both seasonal and annual mean errors in the perfect model runs with glint mode data, but little improvement is obtained when the systematic errors are also considered.

4 Summary and discussion

We have simulated how well X_{CO_2} measurements from the OCO satellite will constrain the surface sources and sinks of CO_2. We used a variational data assimilation technique to do this, treating the measurements at the time and place they occur (at the time step and grid resolution of the transport model) with minimal averaging. The fluxes

are solved at a coarser time resolution – weekly – to get adequate measurement density at our 2°×5° spatial resolution. We have used the best measurement information available: new estimates of single-retrieval error uncertainties and averaging kernels calculated as a function of surface type, aerosol OD, and viewing geometry. And we combine the information from all valid retrievals for each ∼33 s grid box crossing to get the measurement uncertainty used in the assimilation, accounting for correlations in the measurement errors as well as data dropout from clouds and aerosols.

We first computed "best case" flux error estimates from "perfect-model" experiments using X_{CO_2} measurements affected only by random errors. These errors correspond to those that would be given by a covariance matrix. Nadir- and glint-mode measurements give similar flux improvements over the land: generally over 45%/65% for the weekly/seasonal fluxes over the well-vegetated areas with the largest initial flux errors. These weekly flux error reductions are larger than those obtained by Chevallier et al. (2007a) by almost a factor of two, despite the fluxes being solved for at a similar resolution; this is to be expected, since our measurement uncertainties (Fig. 6b) are several times lower than the 2 ppm values they assumed. It is more difficult to compare our results with those of Miller et al. (2007) because they used higher measurement uncertainties (1 ppm) and solved for larger flux regions (effectively adding strong spatial correlations); our flux uncertainties are larger over the land and smaller over the oceans (in both nadir and glint modes). In our simulations, glint mode data give similar land flux error reductions as nadir, despite the larger glint measurement uncertainties over land, apparently because the much more precise glint measurements over the ocean contain a good amount of information on the land fluxes, enough to make up the difference in the land measurements. Over the oceans, the more precise glint measurements lead to much larger flux error reductions than with the nadir data: over 45% across broad swaths of the tropical and southern oceans, versus ∼15% in nadir. Because the glint data provide more of a constraint on the surface fluxes (land plus ocean together), in this view OCO would collect more information overall by remaining in glint mode at all times rather than by switching between glint and nadir modes (but

ACPD
8, 20051–20112, 2008

see discussion below).

If the OCO measurements were affected only by random errors at the levels assumed here, they would constrain the surface CO_2 fluxes much better than the current in situ network (Baker et al., 2006b and Miller et al., 2007 assumed higher measurement errors than used here and still obtained a better constraint with the satellite data over that given by the in situ data). However, there are a variety of systematic errors affecting the assimilation that will prevent the OCO data from reducing the flux errors as much as the perfect-model runs suggest. It is difficult to know beforehand which systematic errors will be most important for a mission; the simple ones that we have added here give only a rough idea of what may actually occur. First of all, we found that mistuning the assimilation (assuming incorrect patterns for the a priori flux error covariance and measurement error covariance matrices) by a modest amount reduces the error reductions by ~10% in many areas. This error source is unavoidable: the assimilation must be constrained by a realistic prior to damp out the worst effects of the random measurement errors (Baker et al., 2006b), and yet there is little chance of modeling the details of the a priori uncertainties correctly to avoid the mistuning (Chevallier et al., 2006); the same modeling challenges apply to the assumed measurement error covariance, too.

Second, we added measurement biases proportional to aerosol OD, since scattering-related errors are expected be an important source of model-measurement mismatches. At the higher of the two levels we examined (a 2 ppm bias per OD), the flux error reductions over the oceans are reduced by at least a factor of two compared with the unbiased values; over land, flux reductions as high as in the unbiased case are still often achieved, but the spatial extent of such reductions are degraded by a factor of two or more. Flux error reductions of over 65% are still achieved in restricted areas over the tropical and northern forests. We obtain aerosol-related annual mean flux biases on the scale of the 22 Transcom3 regions that are generally smaller than Chevallier et al. (2007a) obtain; they are never greater than 0.3 PgC/year and are usually below 0.2 PgC/year. The two largest biases from Chevallier et al. (2007a) (0.73 and

ACPD
8, 20051–20112, 2008

0.57 PgC/year for Temp. Eurasia and Europe, respectively; see their Fig. 4) seem to be due to their use of aerosol biases as high as 1.0 ppm or higher over those regions; our largest biases are only 0.6 ppm here.

Finally, we examined the impact of transport model errors in the assimilation. This was done with an ad hoc approach of shifting the winds used to generate the truth by 17 h. When the transport errors were added without also adding the aerosol biases, we obtained reductions in the 7-day flux improvements similar to those given by the higher of the two aerosol bias experiments (with somewhat lower reductions over the tropical land where the predominantly vertical motions limit errors in the horizontal attribution of the fluxes, and considerably larger reductions over the northern forests where horizontal transport errors plus larger flux variability resulted in stronger horizontal flux attribution errors). The impact on the seasonal flux error reductions was much less: apparently, the transport errors that we added largely average out in time, something that may not occur with more realistic transport errors. When both transport errors and the aerosol biases are added at the same time, the transport errors do degrade the 7-day flux improvements in the extratropics, but this effect is not seen in the seasonal fluxes: the error reductions for the transport plus aerosol bias case is almost as great as with the aerosol biases alone, with reductions of over 45% for most of the well-vegetated areas and reductions of over 65% in more limited areas, notably the southern edges of the tropical rain forests in Africa and America. However, the impact of the combined errors on the oceans is greater: the flux improvements are limited there to only ~20% at best (in glint mode), except for a few small areas in the Tropical Pacific and Southern Ocean.

The assimilations converged in a similar manner across all the experiments: the larger a priori errors were converged first at coarser scales, with the smaller initial errors and finer-scale details being removed later after dozens of iterations of the descent method. Since the largest initial errors tended to be over well-vegetated land areas, these areas were corrected first, with the generally low-flux ocean and desert areas converging later. Furthermore, a trade-off is involved in converging the oceans: some

ACPD
8, 20051–20112, 2008

of the improvement over the vegetated land was lost as the oceans were improved. Our "mistuned" experiment suggests that assimilations of real data, using realistically incorrect a priori flux error covariances, will take 3–4 times longer to converge than our perfect-model runs, at 2°×5° resolution. If finer spatial resolutions are solved for, convergence should take even longer. Thus it is very likely that post-launch OCO flux assimilations will be computationally limited: the assimilations are likely to take so long that they may well need to be cut off before the convergence seen in this paper is achieved. This suggests that even the meager ~20% glint-mode improvement over the oceans noted above will not be achieved unless special measures are taken. To converge the ocean fluxes, we suggest running a coarse resolution assimilation first, followed by a finer-resolution assimilation to give the land fluxes. If the ocean optimization is given up, one could ensure the best convergence over the land by artificially tightening the a priori flux error covariances over the ocean, preventing any initial land improvements from being degraded in an attempt to optimize the oceans.

Our simulations suggest that the precision of OCO's X_{CO_2} measurements is more than adequate for estimating weekly grid-scale CO_2 fluxes at scientifically-useful levels. Knowing annual mean CO_2 fluxes to within 0.1 PgC/yr for most of the 22 Transcom3 regions (Fig. 13) would certainly constrain well the key sources and sinks on a global scale. The real challenge, however, appears to be in identifying and removing systematic errors, both in deriving the X_{CO_2} values and in processing these values with an atmospheric assimilation method. For the level of systematic errors considered here, annual mean flux errors rise as high as 0.2–0.3 PgC/year for many of the Transcom3 regions, a level that, while certainly better than given by the current in situ network, still would leave much uncertainty in the global carbon budget. Since the value of the X_{CO_2} data fall off rapidly if systematic errors are much higher than this, more effort must devoted to quantifying them. We have addressed the systematic errors only in a very rough fashion here. The OCO X_{CO_2} retrievals will likely be corrupted by residual image effects, boresight mis-alignment effects, instrument line shape uncertainties, uncertainties in the measured spectrum, thin-cloud effects, and other errors besides the

ACPD
8, 20051–20112, 2008

aerosol scattering effects considered approximately here. Simulation studies ought to be attempted for all these error sources. These are not simply of academic interest, to be forgotten once the spacecraft begins returning real data; rather, they will be critical for interpreting the data once it arrives. Finally, a more detailed assessment of transport errors must be performed. The transport errors could be quantified by running the identical fluxes (including fossil fuel input at fine spatial scales and diurnally-varying land biospheric fluxes) through multiple transport models, sampling the resulting concentration fields with realistic averaging kernels along realistic OCO orbits, and then comparing the resulting X_{CO_2} values in an approach similar to what the Transcom group has done for continuous in situ and aircraft profile data (Law et al., 2008; Patra et al., 2008; Pickett-Heaps et al., 2008).

Pending these more detailed studies, our simulations suggest that, even when systematic error effects are factored in, the X_{CO_2} data could give improvements in seasonal and annual mean CO_2 fluxes of over 45% over most of sub-Saharan Africa, South America, North America, Siberia, and East Asia. Given the importance that the poorly-known tropical land fluxes are thought to play in driving global CO_2 variability (Baker et al., 2006a) and the continuing uncertainty in the location of the northern CO_2 sink, this new information should greatly improve our knowledge of the functioning of the global carbon cycle.

Appendix A

Cloud coverage calculations

Figure 7b shows the probability of finding at least one cloud-free scene inside an OCO ground track swath of length L, the cloud influence length defined by Eq. (1) and plotted in Fig. 5b. This appendix describes how climatological values for this probability are derived from MODIS observations.

The cloud fraction parameter from the Aqua/MODIS Level 3 MYD08_M3 product

gives the monthly average probability that any single MODIS scene will be clear of detectable clouds, at 1°×1° resolution. This is computed from data at 1 km×1 km resolution, close to the OCO FOV size, and is available for the same orbit as OCO. This should give a very good idea of the probability that any single OCO sounding will see cloud-free conditions. Because of along-track spatio-temporal correlations, however, it is not clear how to compute the probability of finding at least one cloud-free scene in an OCO ground track swath of length L from these single-sounding probabilities. Obtaining that information requires examining the Level 2 MODIS data from which the Level 3 monthly averages were computed.

The Level 2 MODIS data come packaged in the form of "granules", approximately 5 min of measurements spanning roughly 2000 km in the along-track direction and 2330 km across-track (as swept out by a ±55° scan on either side of nadir). Rather than process this massive archive of data ourselves, we used a "climatology" of Level 2 MODIS cloud and cloud mask products (MOD06_L2 and MOD35_L2) that was compiled by Chang and Li (2005), albeit from the Terra satellite which has a somewhat different orbit than Aqua and OCO. To reduce the volume of data to process, Chang and Li processed 8 full days of data in each of the months of January, April, July, and October, spaced 4 days apart from each other. Among other cloud-related quantities, they saved a cloud mask value at 5 km×5 km resolution indicating whether the scene was "cloudy", "possibly cloudy", "probably clear", or "confident clear". For the "cloudy" boxes, an additional value was saved indicating the number of 1 km×1 km pixels inside the 5 km×5 km box (0–25) with measurable cloud optical depths (MODIS can generally detect clouds with ODs as thin as 0.10). This second quantity is valuable because it provides the frequency of occasional cloud gaps in areas with the cloudiest conditions, where OCO will have the most difficulty obtaining data, at a 1 km×1 km resolution that is close to that seen by OCO (nominally 2.7 km^2).

We have sampled the Chang and Li data in 10 km-wide swaths of differing lengths (5, 10, 20, 40, 100, and 200 km) in the along-track direction, accumulating statistics on the probability of finding at least one cloud-free scene at 1 km×1 km resolution inside the

ACPD
8, 20051–20112, 2008

swaths of differing lengths for each month. The probabilities increase with increasing swath length. We normalize the probabilities at each swath length by those at the 5 km length. This normalized multiple represents how many more time likely it is to find at least one 1 km×1 km cloud-free scene in a swath of length L than it is inside a box of 5 km×10 km, accounting for realistic correlations in cloud amount along the track, or cloud "clumpiness". Figure A1a, b gives maps of this multiple interpolated to the actual swath lengths for nadir and glint modes (Fig. 5b) corresponding to the true solar zenith angles around the orbit. At high solar zenith angles, including the near-polar areas where it will be the most difficult to penetrate through the clouds, this multiple is generally over 2.

In the final step of this process, we interpolate these multiples across the full year from the four months examined by Chang and Li, and multiply them by the single-sounding cloud-free probabilities of the Level 3 Aqua/MODIS product (Fig. A1c) to obtain the probability of a cloud-free sounding per cloud correlation length shown in Fig. 5b for the nadir case. For glint mode, these cloud-free probabilities are further reduced to account for the greater path-length in the atmosphere according to Eq. (3) in the main text.

Our approach here is actually somewhat conservative, since the probability of finding a cloud-free sounding inside a box of 5 km×10 km (the value we normalize our Level 2 multiple by) should be higher than the single-sounding cloud-free probability. Another factor to consider is that our Level 2 MODIS multiples are computed using data from the Terra satellite, which has a 10:30 a.m. local ascending node time and thus may not exactly capture the cloud properties that OCO will see in the early afternoon.

Acknowledgements. We wish to express our great appreciation to Fu-Lung Chang of the National Institute for Aerospace, Hampton, VA, for providing us with his Terra/MODIS cloud climatology. SD and DB acknowledge support from NASA grant NNG06G127G. DB also acknowledges initial support from NOAA Grant NA16GP2935.

References

Baker, D. F., Law, R. M., Gurney, K. R., Rayner, P., Peylin, P., Denning, A. S., Bousquet, P., Bruhwiler, L., Chen, Y.-H., Ciais, P., Fung, I. Y., Heimann, M., John, J., Maki, T., Maksyutov, S., Masarie, K., Prather, M., Pak, B., Taguchi, S., and Zhu, Z.: TransCom3 inversion intercomparison: Impact of transport model errors on the interannual variability of regional CO_2 fluxes, 1988–2003, Global Biogeochem. Cy., 20, GB1002, doi:10.1029/2004GB002439, 2006a.

Baker, D. F., Doney, S. C., and Schimel, D. S.: Variational data assimilation for atmospheric CO_2, Tellus B, 58(5), 359–365, doi:10.1111/j.1600-0889.2006.00218.x, 2006b.

Bloom, S., da Silva, A., Dee, D., Bosilovich, M., Chern, J.-D., Pawson, S., Schubert, S., Sienkiewicz, M., Stajner, I., Tan, W.-W., and Wu, M.-L.: Documentation and Validation of the Goddard Earth Observing System (GEOS) Data Assimilation System - Version 4. NASA Technical Report Series on Global Modeling and Data Assimilation 104606, v26, 181 pp., 2005.

Bösch, H., Connor, B., and Baker, D. F.: Global Characterization of X_{CO_2} Retrievals from OCO Observations, in preparation, 2008.

Chang, F.-L. and Li, Z. Q.: A near-global climatology of single-layer and overlapped clouds and their optical properties retrieved from Terra/MODIS data using a new algorithm, J. Climate, 18(22), 4752–4771, 2005.

Chevallier, F., Fisher, M., Peylin, P., Serrar, S., Bousquet, P., Bréon, F.-M., Chédin, A., and Ciais, P.: Inferring CO_2 sources and sinks from satellite observations: Method and application to TOVS data, J. Geophys. Res.-Atmos., 110(D24), D24309, doi:10.1029/2005JD006390, 2005a.

Chevallier, F., Engelen, R. J., and Peylin, P.: The contribution of AIRS data to the estimation of CO_2 sources and sinks, Geophys. Res. Lett., 32(23), L23801, doi:10.1029/2005GL024229, 2005b.

Chevallier, F., Viovy, N., Reichstein, M., and Ciais, P.: On the assignment of prior errors in Bayesian inversions of CO_2 surface fluxes, Geophys. Res. Lett., 33(13), L13802, doi:10.1029/2006GL026496, 2006.

Chevallier, F., Breon, F. M., and Rayner, P. J.: Contribution of the Orbiting Carbon Observatory to the estimation of CO_2 sources and sinks: Theoretical study in a variational data assimilation framework, J. Geophys. Res.-Atmos., 112(D9), D09307, doi:10.1029/2006JD007375,

2007a.
Chevallier, F.: Impact of correlated observation errors on inverted CO_2 surface fluxes from OCO measurements, Geophys. Res. Lett., 34(24), L24804, doi:10.1029/2007GL030463, 2007b.
Connor, B. J., Boesch, H., Toon, G., Sen, B., Miller, C., and Crisp, D.: Orbiting Carbon Observatory: Inverse method and prospective error analysis, J. Geophys. Res.-Atmos., 113, D05305, doi:10.1029/2006JD008336, 2008.
Corbin, K. D, Denning, A. S., Lu, L., Wang, J. W., and Baker, I. T.: Possible representation errors in inversions of satellite CO_2 retrievals, J. Geophys. Res.-Atmos., 113(D2), D02301, doi:10.1029/2007JD008716, 2008.
Crisp, D., Atlas, R. M., Breon, F.-M., Brown, L. R., Burrows, J. P., Ciais, P., Connor, B. J., Doney, S. C., Fung, I. Y., Jacob, D. J., Miller, C. E., O'Brien, D., Pawson, S., Randerson, J. T., Rayner, P., Salawitch, R. J., Sander, S. P., Sen, B., Stephens, G. L., Tans, P. P., Toon, G. C., Wennberg, P. O., Wofsy, S. C., Yung, Y. L., Kuang, Z., Chudasama, B., Sprague, G., Weiss, B., Pollock, R., Kenyon, D., and Schroll, S.: The Orbiting Carbon Observatory (OCO) Mission, Adv. Space Res., 34, 700–709, 2004.
Doney, S. C., Lindsay, K., Caldeira, K., Campin, J.-M., Drange, H., Dutay, J.-C., Follows, M., Gao, Y., Gnanadesikan, A., Gruber, N., Ishida, A., Joos, F., Madec, G., Maier-Reimer, E., Marshall, J. C., Matear, R. J., Monfray, P., Mouchet, A., Najjar, R., Orr, J. C., Plattner, G.-K., Sarmiento, J., Schlitzer, R., Slater, R., Totterdell, I. J., Weirig, M.-F., Yamanaka, Y., and Yool, A.: Evaluating global ocean carbon models: the importance of realistic physics, Global Biogeochem. Cy., 18, GB3017, doi:10.1029/2003GB002150, 2004.
Enting, I. G., Trudinger, C. M., Francey, R. J., and Granek, H.: A synthesis inversion of the concentration and $\delta^{13}C$ of atmospheric CO_2, Tellus B, 47, 35–52, 1995.
Gerbig, C., Lin, J. C., Wofsy, S. C., Daube, B. C., Andrews, A. E., Stephens, B. B., Bakwin, P. S., and Grainger, C. A.: Toward constraining regional-scale fluxes of CO_2 with atmospheric observations over a continent: 2. Analysis of COBRA data using a receptor-oriented framework, J. Geophys. Res., 108(D24), 4757, doi:10.1029/2003JD003770, 2003.
Houweling, S., Breon, F.-M., Aben, I., Rödenbeck, C., Heimann, M., and Ciais, P.: Inverse modelling of CO_2 sources and sinks using satellite data: a synthetic inter-comparison of measurement techniques and their performance as a function of space and time, Atmos. Chem. Phys., 4, 523–538, 2004, http://www.atmos-chem-phys.net/4/523/2004/.
Kawa, S. R., Erickson, D. J., Pawson, S., and Zhu, Z.: Global CO_2 transport simulations using meteorological data from the NASA data assimilation system, J. Geophys. Res.-Atmos.,

109(D18), D18312, doi:10.1029/2004JD004554, 2004.
Law, R. M., Peters, W., Rodenbeck, C., Aulagnier, C., Baker, I., Bergmann, D. J., Bousquet, P., Brandt, J., Bruhwiler, L., Cameron-Smith, P. J., Christensen, J. H., Delage, F., Denning, A. S., Fan, S., Geels, C., Houweling, S., Imasu, R., Karstens, U., Kawa, S. R., Kleist, J., Krol, M. C., Lin, S.-J., Lokupitiya, R., Maki, T., Maksyutov, S., Niwa, Y., Onishi, R., Parazoo, N., Patra, P. K., Pieterse, G., Rivier, L., Satoh, M., Serrar, S., Taguchi, S., Takigawa, M., Vautard, R., Vermeulen, A. T., and Zhu, Z: TransCom model simulations of hourly atmospheric CO_2: experimental overview and diurnal cycle results for 2002, Global Biogeochem. Cy., GB3009, doi:10.1029/2007GB003050, 2008.
Lin, J. C., Gerbig, C., Wofsy, S. C, Andrews, A. E., Daube, B. C., Grainger, C. A., Stephens, B. B., Bakwin, P. S., and Hollinger, D. Y.: Measuring fluxes of trace gases at regional scales by Lagrangian observations: Application to the CO_2 Budget and Rectification Airborne (COBRA) study, J. Geophys. Res., 109, D15304, doi:10.1029/2004JD004754, 2004.
Lin, S.-J.: A vertically Lagrangian finite-volume dynamical core for global models, Mon. Weather Rev., 132, 2293–2307, 2004
Meirink, J. F., Bergamaschi, P., Frankenberg, C., d'Amelio, M. T. S., Dlugokencky, E. J., Gatti, L. V., Houweling, S., Miller, J. B., Röckmann, T., Villani, M. G., and Krol, M. C.: Four-dimensional Variational Data Assimilation for Inverse Modelling of Atmospheric Methane Emissions: 2. Analysis of SCIAMACHY Observations, J. Geophys. Res.-Atmos., doi:10.1029/2007JD009740, 2008.
Miller, C. E., Crisp, D., DeCola, P. L., Olsen, S. C., Randerson, J. T., Michalak, A. M., Alkhaled, A., Rayner, P., Jacob, D. J., Suntharalingam, P., Jones, D. B. A., Denning, A. S., Nicholls, M. E., Doney, S. C., Pawson, S., Boesch, H., Connor, B. J., Fung, I. Y., O'Brien, D., Salawitch, R. J., Sander, S. P., Sen, B., Tans, P., Toon, G. C., Wennberg, P. O., Wofsy, S. C., Yung, Y. L., and Law, R. M.: Precision requirements for space-based X-CO_2 data, J. Geophys. Res.-Atmos., 112(D10), D10314, doi:10.1029/2006JD007659, 2007.
Najjar, R. G., Jin, X., Louanchi, F., Aumont. O., Caldeira, K., Doney, S. C., Dutay, J.-C., Follows, M., Gruber, N., Joos, F., Lindsay, K., Maier-Reimer, E., Matear, R. J., Matsumoto, K., Monfray, P., Mouchet, A., Orr, J. C., Plattner, G.-K., Sarmiento, J. L., Schlitzer, R., Slater, R. D., Weirig, M.-F., Yamanaka, Y., and Yool, Y.: Impact of circulation on export production, dissolved organic matter, and dissolved oxygen in the ocean: Results from Phase II of the Ocean Carbon-cycle Model Intercomparison Project (OCMIP-2), Global Biogeochem. Cy., 21, GB3007, doi:10.1029/2006GB002857, 2007.

Olsen, S. C. and Randerson, J. T.: Differences between surface and column atmospheric CO_2 and implications for carbon cycle research, J. Geophys. Res.-Atmos., 109(D2), D02301, doi:10.1029/2003JD003968, 2004.

Patra, P. K., Maksyutov, S., Ishizawa, M., Nakazawa, T., Takahashi, T., and Ukita, J.: Interannual and decadal changes in the sea-air CO_2 flux from atmospheric CO_2 inverse modeling, Global Biogeochem. Cy., 19, GB4013, doi:10.1029/2004GB002257, 2005.

Patra, P. K., Law, R. M., Peters, W., Rodenbeck, C., Takigawa, M., Aulagnier, C., Baker, I., Bergmann, D. J., Bousquet, P., Brandt, J., Bruhwiler, L., Cameron-Smith, P. J., Christensen, J. H., Delage, F., Denning, A. S., Fan, S., Geels, C., Houweling, S., Imasu, R., Karstens, U., Kawa, S. R., Kleist, J., Krol, M. C., Lin, S.-J., Lokupitiya, R., Maki, T., Maksyutov, S., Niwa, Y., Onishi, R., Parazoo, N., Pieterse, G., Rivier, L., Satoh, M., Serrar, S., Taguchi, S., Vautard, R., Vermeulen, A. T., and Zhu, Z.: TransCom model simulations of hourly atmospheric CO_2: Analysis of synoptic-scale variations for the period 2002–2003, Global Biogeochem. Cy., 22, GB4013, doi:10.1029/2007GB003081, 2008.

Peters, W., Miller, J. B., Whitaker, J., Denning, A. S., Hirsch, A., Krol, M. C., Zupanski, D., Bruhwiler, L., and Tans, P. P.: An ensemble data assimilation system to estimate CO_2 surface fluxes from atmospheric trace gas observations, J. Geophys. Res.-Atmos., 110(D24), D24304, doi:10.1029/2005JD006157, 2005.

Peylin, P., Rayner, P. J., Bousquet, P., Carouge, C., Hourdin, F., Heinrich, P., Ciais, P., and AEROCARB contributors: Daily CO_2 flux estimates over Europe from continuous atmospheric measurements: 1, Inverse methodology, Atmos. Chem. Phys., 5, 3173–3186, 2005a, http://www.atmos-chem-phys.net/5/3173/2005/.

Peylin, P., Bousquet, P., Le Quéré, C., Sitch, S., Friedlingstein, P., McKinley, G., Gruber, N., Rayner, P., and Ciais, P.: Multiple constraints on regional CO_2 flux variations over land and oceans, Global Biogeochem. Cy., 19(1), GB1011, doi:10.1029/2003GB002214, 2005b.

Pickett-Heaps, C. A., Rayner, P. J., Law, R. M., Bousquet, P., Peylin, P., Patra, P., Maksyutov, S., Marshall, J., Roedenbeck, C., Ciais, P., Langenfelds, R., Tans, P., Steele, P., and Francey, R.: Atmospheric CO_2 inversion cross-validation using vertical profile measurements, J. Geophys. Res., in press, 2008.

Randerson, J. T., Thompson, M. V., Conway, T. J., Fung, I. Y., and Field, C. B.: The contribution of terrestrial sources and sinks to trends in the seasonal cycle of atmospheric carbon dioxide, Global Biogeochem. Cy., 11, 535–560, 1997.

Rayner, P. J., and O'Brien, D.: The utility of remotely sensed CO_2 concentration data in surface

ACPD

8, 20051–20112, 2008

source inversions, Geophys. Res. Lett., 28, 175–178, 2001.
Rayner, P. J., Scholze, M., Knorr, W., Kaminski, T., Giering, R., and Widmann, H.: Two decades of terrestrial carbon fluxes from a carbon cycle data assimilation system (CCDAS), Global Biogeochem. Cy., 19, GB2026, doi:10.1029/2004GB002254, 2005.
Rayner P. J., Law, R. M., Allison, C. E., Francey, R. J., Trudinger, C. M., and Pickett-Heaps, C.: Interannual variability of the global carbon cycle (1992–2005) inferred by inversion of atmospheric CO_2 and $\delta^{13}CO_2$ measurements, Global Biogeochem. Cy., 22, GB3008, doi:10.1029/2007GB003068, 2008.
Rödenbeck, C., Houweling, S., Gloor, M., and Heimann, M.: CO_2 flux history 1982-2001 inferred from atmospheric data using a global inversion of atmospheric transport, Atmos. Chem. Phys., 3, 1919–1964, 2003, http://www.atmos-chem-phys.net/3/1919/2003/.
Rödenbeck, C.: Estimating CO_2 sources and sinks from atmospheric mixing ratio measurements using a global inversion of atmospheric transport, Max-Planck-Institut für Biogeochemie: Technical Paper 6, http://www.bgc-jena.mpg.de/mpg/websiteBiogeochemie/Publikationen/Technical_Reports/tech_report6.pdf, 2005.
Sitch, S., Smith, B., Prentice, I. C., Arneth, A., Bondeau, A., Cramer, W., Kaplan, J. O., Levis, S., Lucht, W., Sykes, M. T., Thonicke, K., and Venevsky, S.: Evaluation of ecosystem dynamics, plant geography and terrestrial carbon cycling in the LPJ dynamic global vegetation model, Glob. Change Biol., 9(2), 161–185, 2003.
Takahashi, T., Wanninkhof, R. H., Feely, R. A., Weiss, R. F., Chipman, D. W., Bates, N., Olafsson, J., Sabine, C., and Sutherland, S. C.: Net sea-air CO_2 flux over the global oceans: an improved estimate based on the sea-air pCO_2 difference, in: Proceedings of the 2nd International Symposium: CO_2 in the Oceans, the 12th Global Environmental Tsukuba, 18–22 January 1999, Tsukuba Center of Institutes, edited by: Nojiri, Y., Natl. Inst. for Envir. Studies, Envir. Agency of Japan, 9–15, 1999.
Zupanski, D., Denning, A. S., Uliasz, M., Zupanski, M., Schuh, A. E., Rayner, P. J., Peters, W., and Corbin, K. D.: Carbon flux bias estimation employing maximum likelihood ensemble filter (MLEF), J. Geophys. Res.-Atmos., 112(D17), D17017, doi:10.1029/2006JD008371, 2007.

ACPD
8, 20051–20112, 2008

Table 1. The errors added to the true measurements and the random error sources assumed in the assimilation are given here for the various OSSEs. Figure numbers are given for annual summary plots of the various added or assumed errors (e.g., "5b"). N=nadir, G=glint. Figure 2d shows the absolute value of the actual prior-truth flux differences; since these differences were used to set the assumed a priori covariance matrix in all the assimilations except #3, only in that case was the a priori error "mistuned". In all experiments, the spatial representation errors in Fig. 6c were added both to the measurement noise on the true measurements and to the assumed measurement uncertainties.

Experiment Description	Exp. No.	Nadir /Glint	Added and Assumed Meas Noise	Prior Flux Uncert. Assumed	Aerosol Bias Added	Aerosol Noise Assumed	Transport Error Added√	Transport Noise Assumed
Perfect Model	1	N	5b, 5b	2d				
Perfect Model	2	G	5b, 5b	2d				
Mistuned	3	G	5d, 5b	2e				
Aerosol bias	4	G	5b, 5b	2d	1x	5e		
2xAerosol bias	4b	G	5b, 5b	2d	2x	2x5e		
Transport error	5	G	5b, 5b	2d			√	5f
Aero + Transport	6	G	5b, 5b	2d	1x	5e	√	5f
2xAero+Transport	6b	G	5b, 5b	2d	2x	2x5e	√	5f

ACPD
8, 20051–20112, 2008

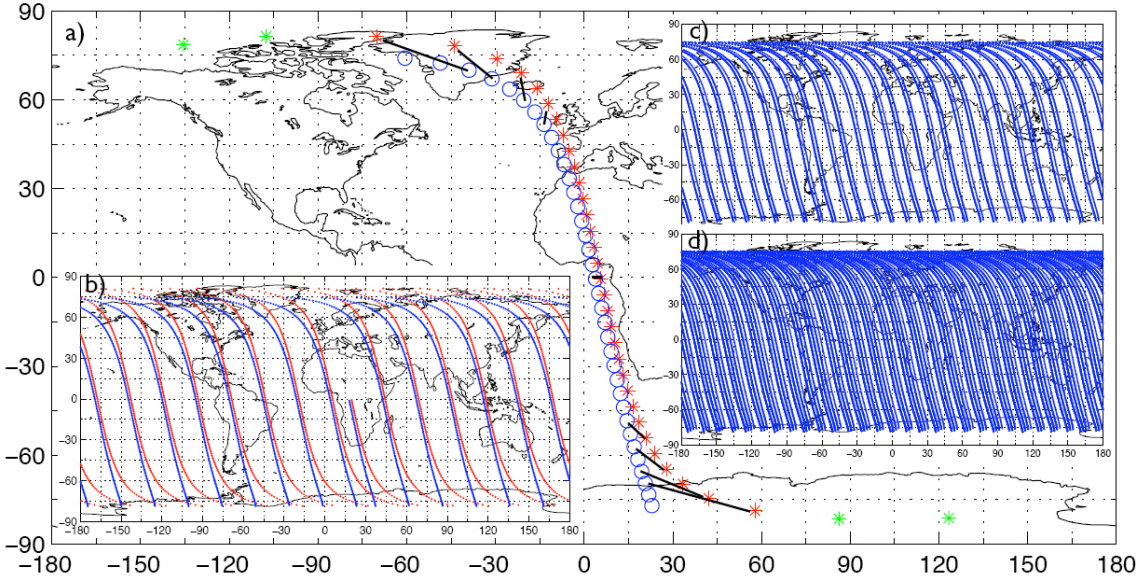

Fig. 1.

ACPD

8, 20051–20112, 2008

Carbon flux information from OCO column CO_2 measurements

D. F. Baker et al.

Fig. 1. (a) An example of the field-of-view ground tracks for OCO for 21 March: 100 min of measurement locations in rotating Earth frame, for nadir pointing mode (asterisks) and glint (circles), with symbols plotted every 90 s for all sun-lit times when the glint-mode SZA≤80°. The shift towards the sun position from nadir to glint can be seen by comparing symbols plotted at the same times (some examples are connected with black lines). The green asterisks indicate the position of the satellite when the nadir-mode SZA≥85° and the glint-mode SZA≤80°. **(b)** One full day's coverage for 21 March for nadir mode (red) with SZA≤85° and glint mode (blue) with SZA≤80°. **(c)** Four- and **(d)** seven-day coverage for glint mode beginning 21 March. Symbols are plotted every 20 s in panels (b–d).

ACPD

8, 20051–20112, 2008

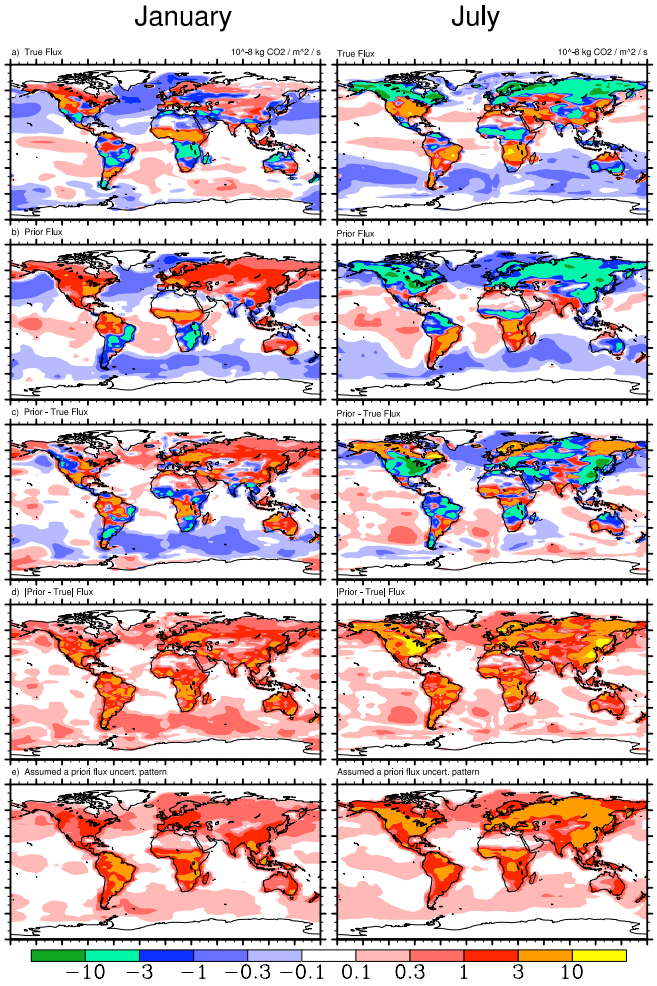

Fig. 2.

ACPD
8, 20051–20112, 2008

Carbon flux information from OCO column CO_2 measurements

D. F. Baker et al.

Fig. 2. January (left) and July (right) mean values for **(a)** the "true" surface CO_2 fluxes used in generating the measurements (land fluxes from the LPJ terrestrial ecosystem model, ocean fluxes from the NCAR ocean biogeochemistry model); **(b)** the a priori CO_2 fluxes assumed in the simulation, both as a constraint in the cost function and as the starting point of the optimization (land fluxes from the CASA land biosphere model, ocean fluxes from Takahashi et al., 1999); **(c)** the prior-truth flux difference; **(d)** the absolute value of (c) – these values are used in the assumed a priori flux error covariance matrix for all experiments except Experiment 3; and **(e)** the corresponding uncertainties used in Experiment 3, the mistuning experiment.

ACPD

8, 20051–20112, 2008

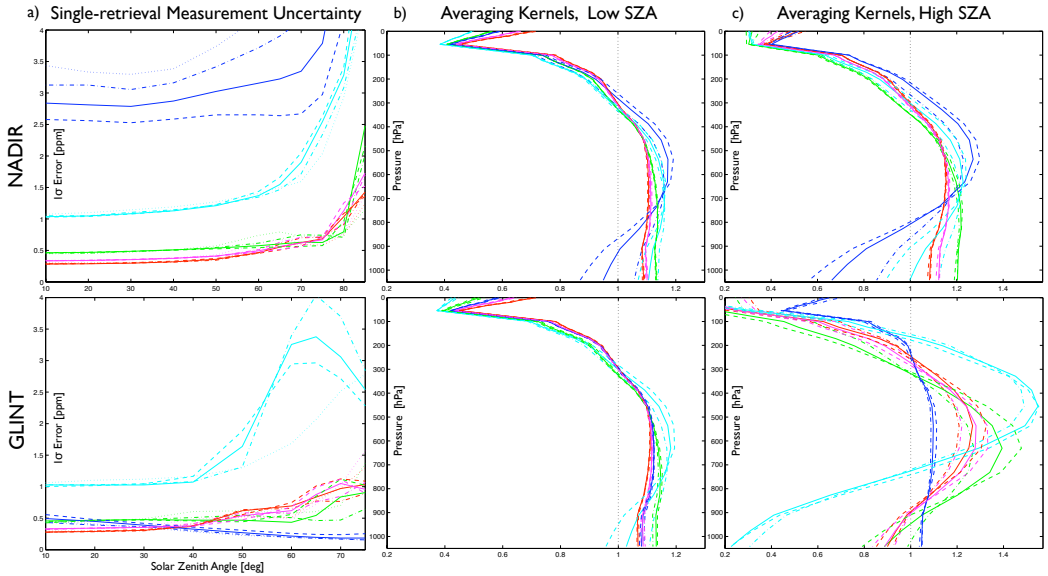

Fig. 3. A summary of **(a)** the single-sounding OCO X_{CO_2} uncertainties [ppm] and **(b–c)** averaging kernels (AKs) used here for measurements taken in nadir mode (top) and glint mode (bottom), given by new radiative transfer simulations performed using the OCO full-physics retrieval algorithm (Bösch et al., 2008) Both are given for five surface types (**conifer**, green; **desert**, red; **sparse vegetation**, magenta; **snow**, cyan; and **ocean**, blue) and for three 760 nm aerosol ODs optical depth (0.10, dot-dash; 0.20, solid; and 0.30, dashed lines); a 0.00 (OD) contour is also given for the uncertainties (dotted line). The AKs in **(b)** have been averaged over SZAs of 20°, 30°, 40°, and 50°, while those in **(c)** are averaged over SZAs of 60°, 65°, 70°, and 75° for glint mode, and 60°, 65°, 70°, 75°, and 80° for nadir mode. All the AKs are normalized by pressure.

ACPD
8, 20051–20112, 2008

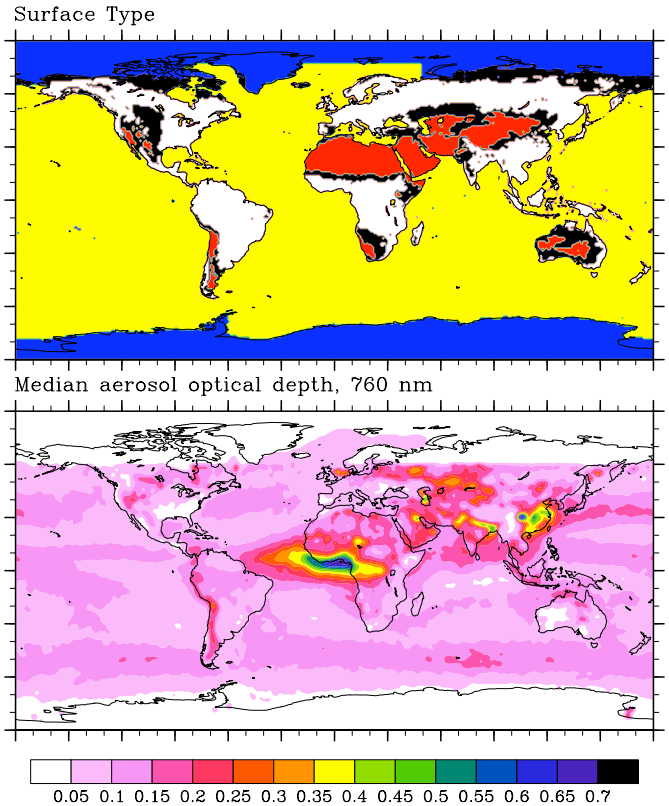

Fig. 4. **(a)** The distribution of the 5 surface cover types, at 1°×1° resolution: desert (red), conifer (white), ocean/water (yellow), snow (blue), and soil/sparse vegetation (black). **(b)** The median aerosol OD at 760 nm (the wavelength of the O_2 A-band used to compute the pressure) at 1°×1° resolution, computed from Aqua/MODIS data according to the procedure outlined in Bösch et al. (2008). The median aerosol ODs are computed from the mean of the four seasonal medians, while the surface types do not vary in time.

ACPD
8, 20051–20112, 2008

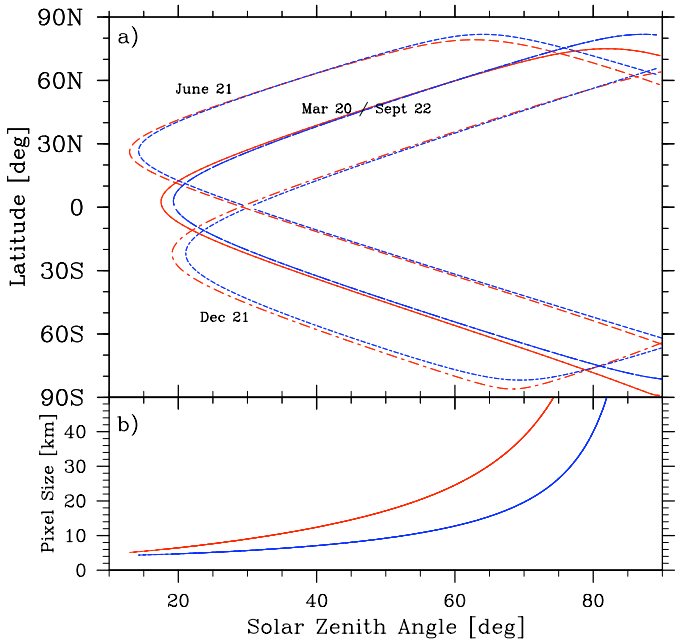

Fig. 5. (a) The solar zenith angles (SZAs) encountered by the OCO spacecraft in nadir pointing mode (blue) and glint mode (red) at four times, i) 21 June, ii) 20 March and 22 September (same solar declination) and iii) 21 December, plotted against the latitude of the FOV location, assuming a 13:18 local time for the ascending node. The maximum SZA is taken as 85° for nadir and 80° for glint viewing modes in the assimilation. (Note that the FOV latitude may turn back towards the equator at high SZAs near the time of the solstices. As shown in Fig. 1a, the actual spacecraft latitude can be quite different than the FOV latitude in glint mode: at high SZAs, the spacecraft may well be flying over a dark portion of the Earth while looking at a lit glint point.) **(b)** The length scale L across which measurement errors are assumed to be independent, for nadir (blue) and glint (red) pointing modes, as given by Eq. (1).

ACPD
8, 20051–20112, 2008

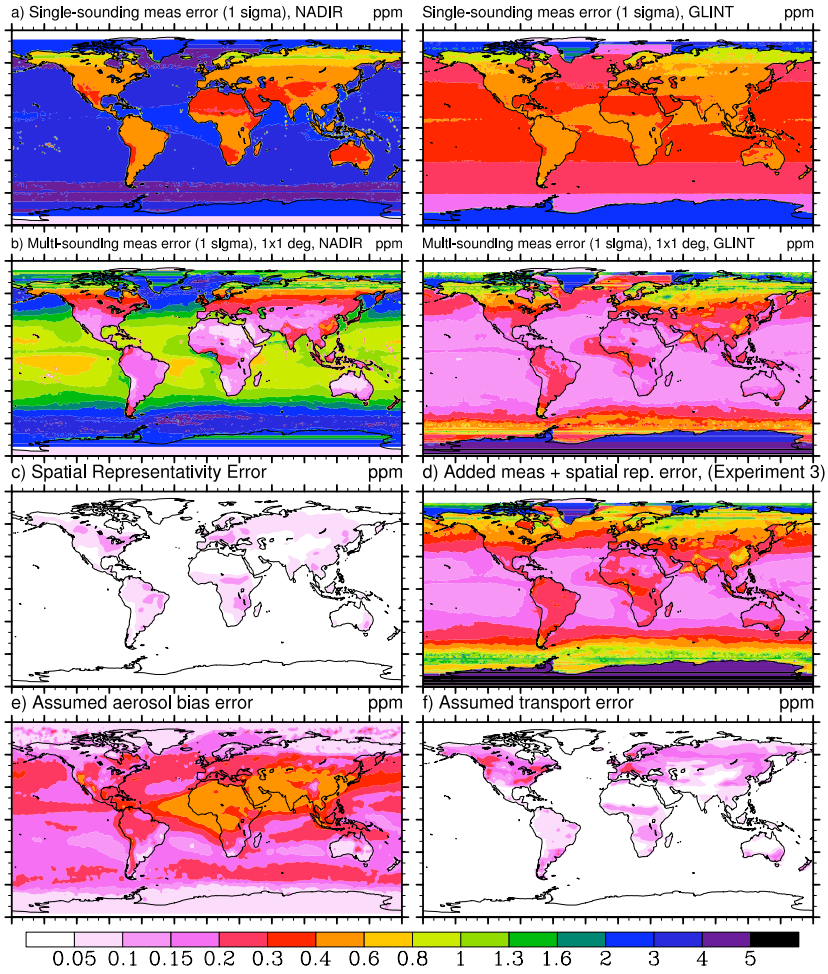

Fig. 6.

ACPD
8, 20051–20112, 2008

Carbon flux information from OCO column CO_2 measurements

D. F. Baker et al.

Fig. 6. **(a)** The single-sounding OCO X_{CO_2} retrieval uncertainties σ_{1_shot} computed in Bösch et al. (2008), mapped onto a 1°×1° grid using SZAs computed for realistic orbital geometries (Figs. 1 and 5a), surface types and median aerosol ODs (Fig. 4), for both nadir (left) and glint (right) viewing modes. **(b)** The effective multi-sounding OCO X_{CO_2} measurement uncertainty σ_{eff} for all valid retrievals inside each 1° latitude band along a single sun-lit pass of the OCO orbit, computed using the single-sounding uncertainties σ_{1_shot} from Fig. 6a and the effective number of independent measurements N_{eff} from Fig. 7a as $\sigma_{eff}=\sigma_{1\_shot}/\sqrt{N_{eff}}$. **(c)** The assumed spatial representation error, extrapolated from the two sites in Corbin et al. (2008) with a pattern proportional to the a priori net flux magnitudes. **(d)** The measurement error added to the data (in place of the glint errors in Fig. 6b) in Experiment 3, the mistuning experiment. **(e)** The uncertainty added in quadrature to the assumed measurement uncertainties to account for the impact of aerosol biases in those experiments in which those biases are added (Experiments 4 and 6; 4b and 6b add twice this). **(f)** The uncertainty added to the assumed measurement uncertainties to account for the impact of transport errors in those experiments in which they are added (Exps. 5 and 6).

ACPD

8, 20051–20112, 2008

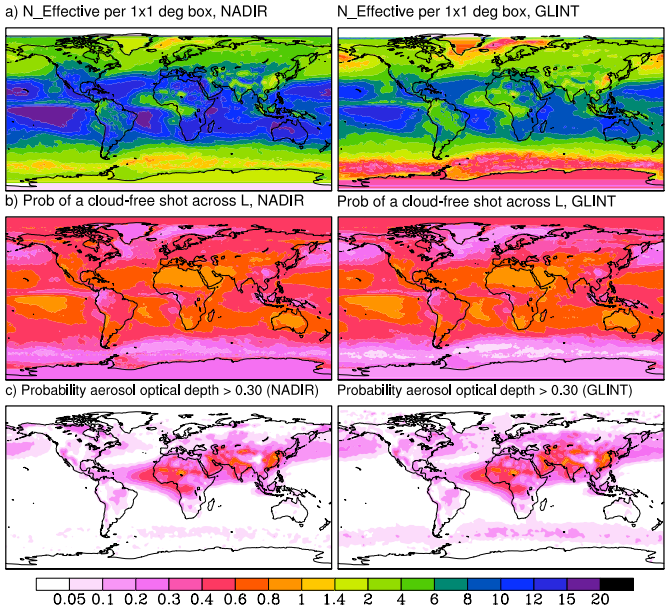

Fig. 7. **(a)** The effective number of independent X_{CO_2} measurements N_{eff} in each 1° latitude band for a single sun-lit pass of the OCO orbit for both nadir (left) and glint (right), computed with Eq. (2) using realistic SZAs (Fig. 5a), cloud-free probabilities (Fig. 7b), and high aerosol OD probabilities (Fig. 7c). **(b)** The probability $P_{cloud-free}$ of finding at least one cloud-free X_{CO_2} measurement inside a portion of the OCO FOV ground track of length L (Fig. 5b), calculated from MODIS data according to the procedure outlined in the Appendix. **(c)** The probability $P_{HiAeroOD}$ of encountering aerosol ODs at 760 nm of greater than 0.30 (the cutoff beyond which X_{CO_2} retrievals are not attempted), computed from Aqua/MODIS data according to the procedure given in Bösch et al. (2008). Annual RMS values are given across that portion of the year that measurements are available for all fields shown in this figure. Measurements from the sunlit portion of the backside of the orbits are used in the assimilation, but are not included in the values computed for this figure.

ACPD
8, 20051–20112, 2008

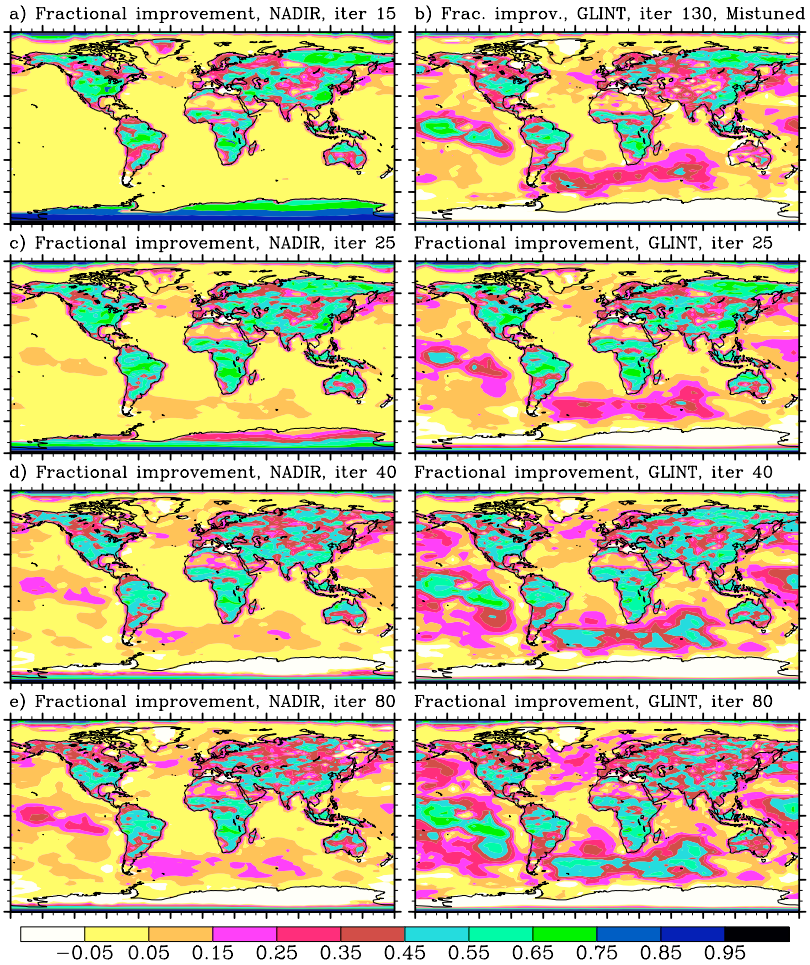

Fig. 8.

ACPD
8, 20051–20112, 2008

Carbon flux information from OCO column CO_2 measurements

D. F. Baker et al.

Fig. 8. Fractional error reductions in 7-day CO_2 fluxes, computed across full annual cycle from the perfect model experiment RMS flux differences for nadir mode (left) and glint mode (right) after **(c)** 25, **(d)** 40, and **(e)** 80 iterations of the optimization method. **(a)** The corresponding nadir mode results after 15 iterations. **(b)** The results from iteration 130 of Experiment 3, the glint mode experiment in which the assumed a priori flux and measurement error covariance matrices are mistuned. Because the mistuning slows the convergence of the optimization, iteration 130 of Experiment 3 is about as far along the convergence trajectory as iteration 40 of Experiment 2.

ACPD

8, 20051–20112, 2008

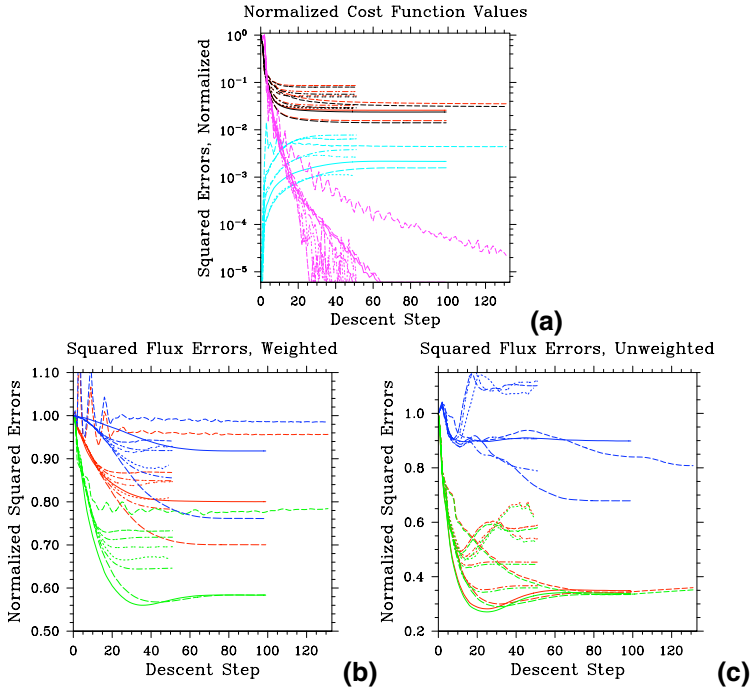

Fig. 9. The convergence of the assimilation results as a function of descent iteration count for Experiments #1 (solid), #2 (long dash), #3 (medium dash), #4 (dot-dash), #4b (dot-dot-dash), #5 (dotted), #6 (double short dash), and #6b (double medium dash) all normalized by the initial values before the assimilation. **(a)** total cost function value (red), measurement portion of cost function (black), prior portion of cost function (blue), and change in cost function value (magenta); **(b)** estimate-truth global 7-day flux errors squared, weighted by the inverse of the assumed a priori flux error covariance, for land (green), ocean (blue), and land+ocean (red); **(c)** estimate-truth global 7-day flux errors squared, unweighted, for land (green), ocean (blue), and land+ocean (red).

ACPD
8, 20051–20112, 2008

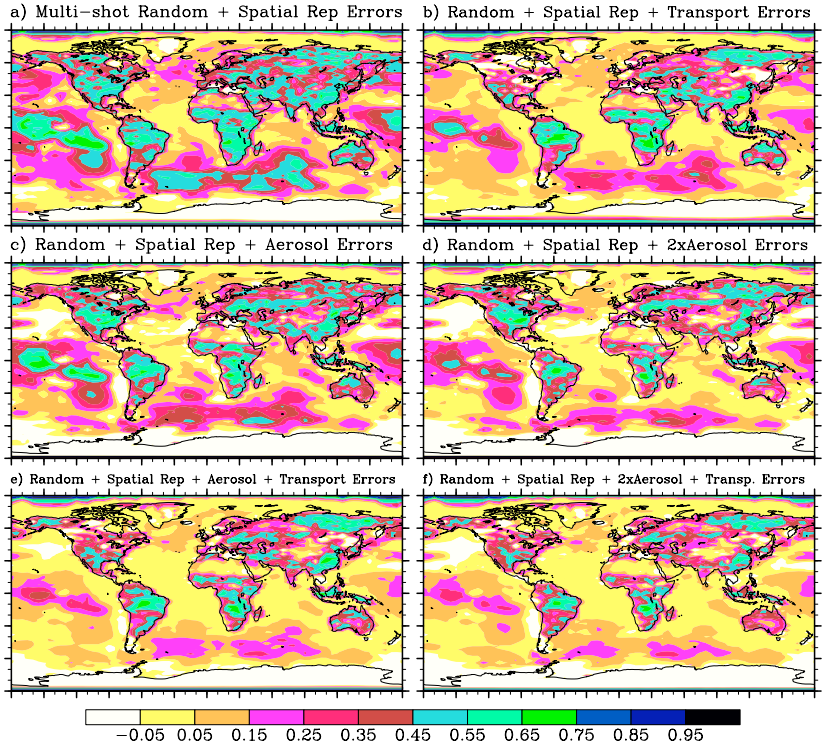

Fig. 10. Fractional error reductions in 7-day CO_2 fluxes, using RMS errors computed across full annual cycle, for glint mode data after 50 iterations for the following experiments: **(a)** #2, perfect model simulation considering multi-sounding random measurement errors and spatial representation errors; **(b)** #5, random measurement errors, spatial representation errors, and transport errors; **(c)** and **(d)** #4 and #4b, random measurement errors, spatial representation errors, and 1x/2x aerosol biases; and **(e)** and **(f)** #6 and #6b, random measurement errors, spatial representation errors, 1x/2x aerosol biases, and transport errors.

ACPD
8, 20051–20112, 2008

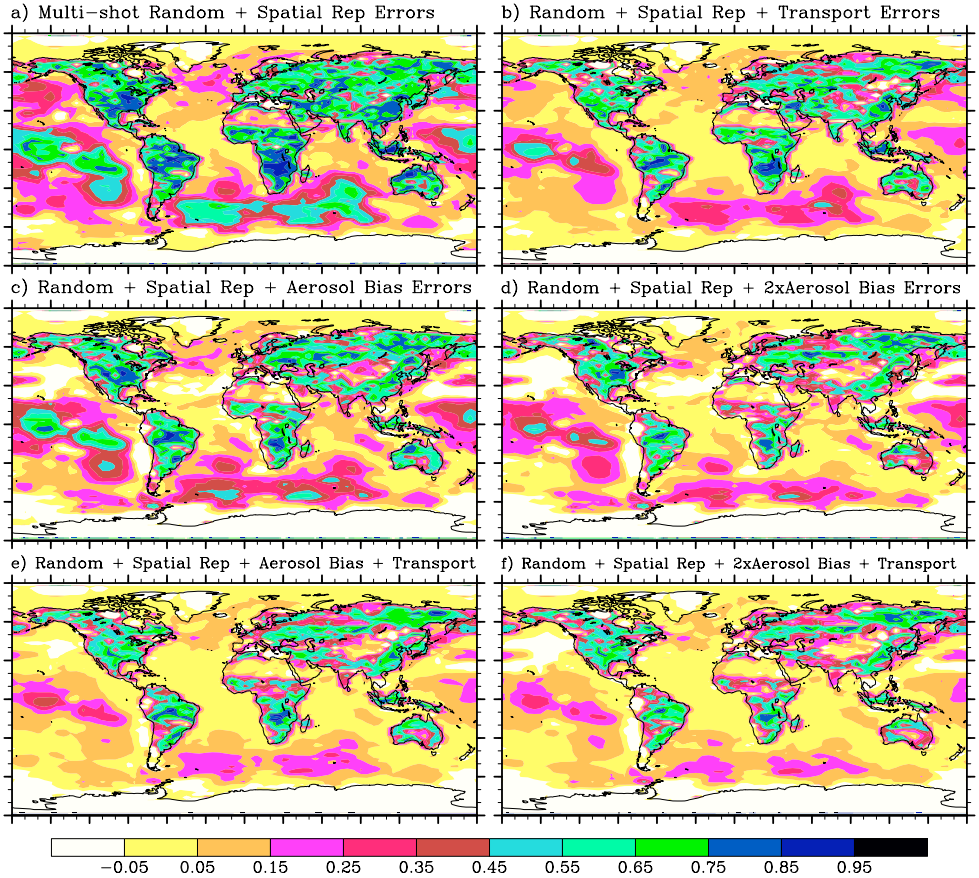

Fig. 11. Fractional error reductions in seasonal CO_2 fluxes, computed from the RMS of the four seasonal values (JFM, AMJ, JAS, OND) using glint mode data after 50 iterations for the following experiments: **(a)** #2, **(b)** #5, **(c)** #4, **(d)** #4b, **(e)** #6, and (f) #6b, as in Fig. 10.

ACPD
8, 20051–20112, 2008

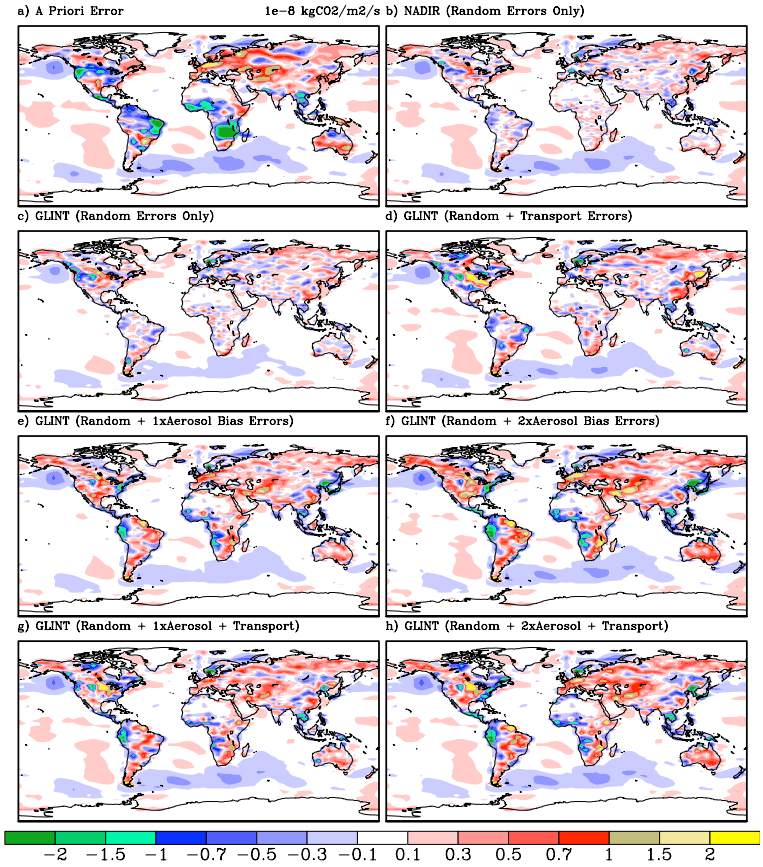

Fig. 12. Annual mean flux errors (10^{-8} $kgCO_2$ m^{-2} s^{-1}) using glint mode data after 50 iterations for the following experiments: **(c)** #2, **(d)** #5, **(e)** #4, **(f)** #4b, **(g)** #6, and **(h)** #6(b). Also, **(a)** the a priori flux difference and **(b)** annual mean flux errors given using nadir mode data after 50 iterations are given, as well.

ACPD
8, 20051–20112, 2008

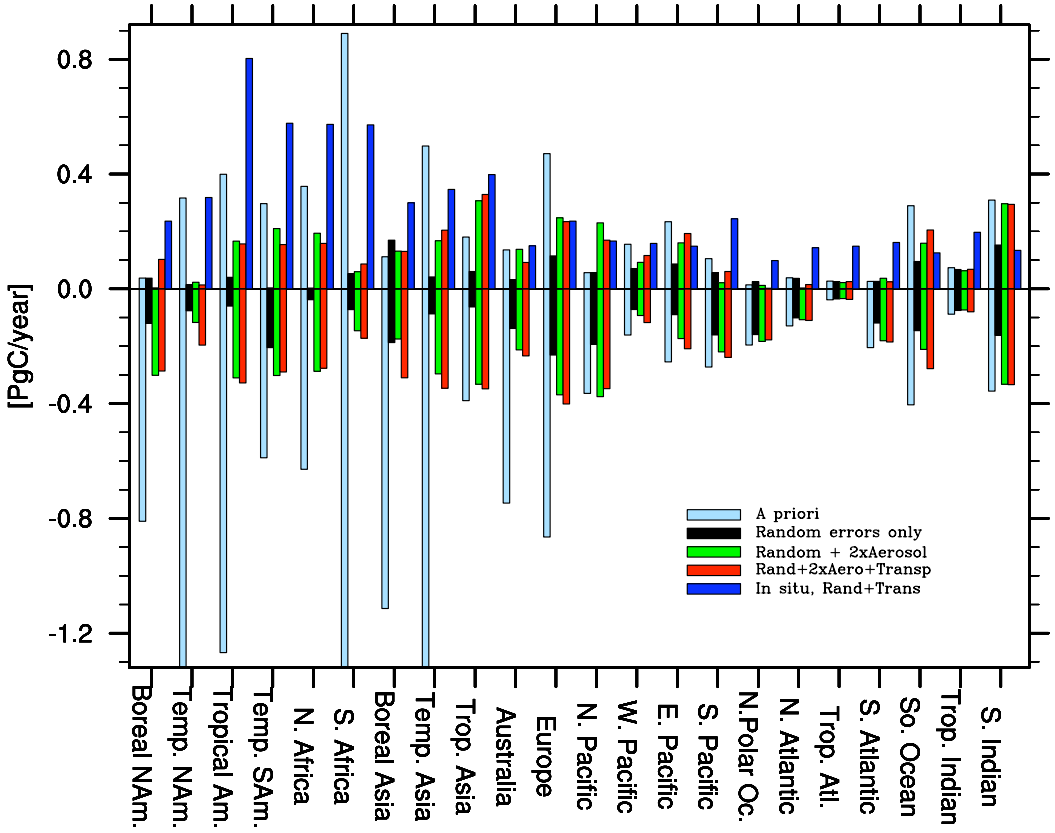

Fig. 13.

ACPD
8, 20051–20112, 2008

Fig. 13. Annual mean flux errors and RMS seasonal flux errors [PgC/year] integrated over the areas of the 22 Transcom3 emission regions. The absolute values of the annual mean errors are plotted on top as positive values, while the RMS of four 13-week seasonal values are plotted below as negative values. A posteriori errors from three glint mode experiments are given: #2 (black bars) in which only random measurement and spatial representativity errors added, #4b (green) in which both random measurement and 2x aerosol bias errors are added, and #6b (red) in which random, 2x aerosol bias, and transport errors are all added. Also given: the a priori flux errors (light blue) and the a posteriori errors given using only data from the in situ CO_2 montoring network of the 1990s (dark blue), computed as the root sum square of the "Post. Error" and "Model Error" columns from Table 4 of the Transcom3 CO_2 flux interannual variability study (Baker et al., 2006a). See Fig. 1 from Baker et al. (2006a) for a map of the 22 emission regions. Note that the Transcom3 in situ errors should be increased, when being compared to the results from this study, to account for the impact of assuming fixed flux patterns inside each of the 22 emission regions in the Transcom3 flux inversions; this extra information acts as an additional prior constraint not included in the present study, which assumed fixed flux patterns across only the $2^{\circ}\times5^{\circ}$ transport grid boxes.

ACPD
8, 20051–20112, 2008

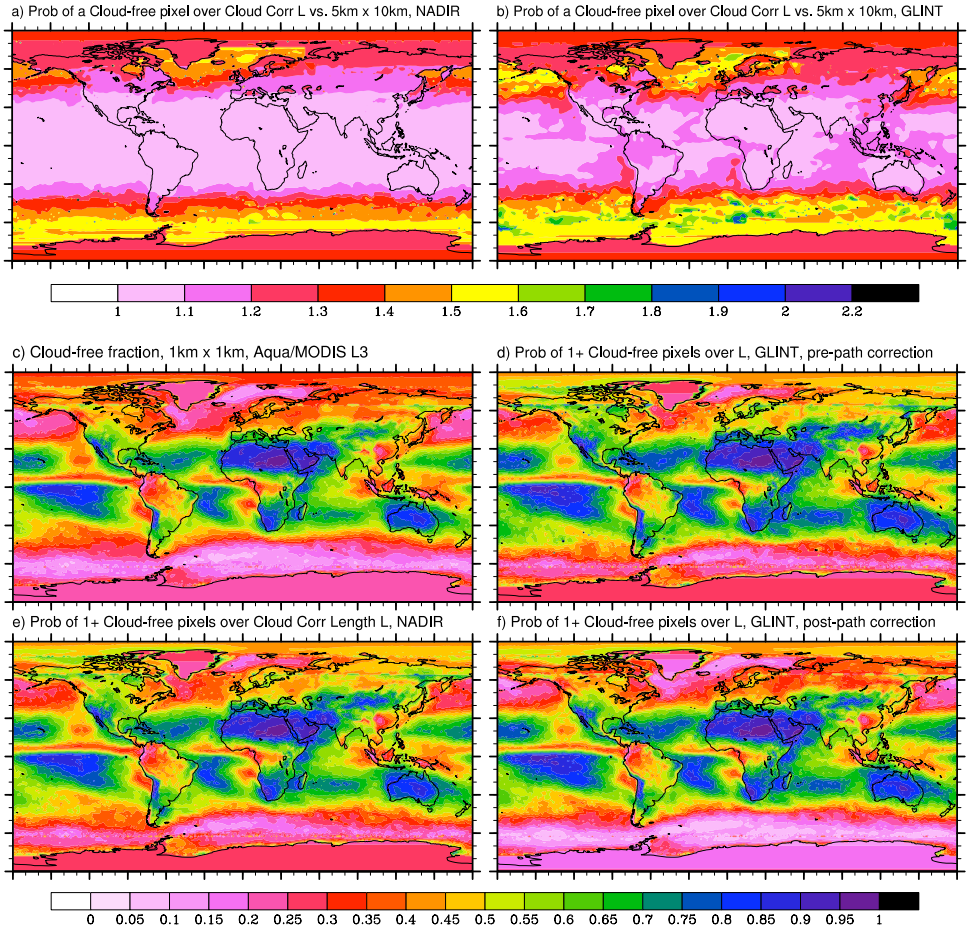

Fig. A1.

ACPD
8, 20051–20112, 2008

Fig. A1. Computation of climatological cloud-free pixel availability from Terra/MODIS and Aqua/MODIS data. **(a)** and **(b)**: The ratio of the probability of finding at least one cloud-free sounding across a ground track swath one cloud correlation length L long (Fig. 5b) over the same probability for a swath only 5 km long, calculated by sampling 10 km-wide Terra/MODIS Level 2 data swaths in the along-track direction, using cloud correlation lengths for nadir- and glint-viewing modes, respectively. **(c)** The cloud-free probability at 1 km×1 km resolution, taken from the Aqua/MODIS Level 3 data cloud-mask product. **(d)** and **(e)**: The probability of finding at least one cloud free sounding in an OCO ground track swath one cloud correlation length L long, for glint and nadir modes, respectively, found by multiplying the fine-resolution Aqua/MODIS cloud-free probabilities from (c) by the ratios in (b) and (a). **(f)** The glint-mode cloud-free probability from (d) corrected for the greater atmospheric path length at high SZAs seen by OCO according to Eq. (3) in the text. Note that because the cloud correlation length is almost twice as long in glint mode as in nadir at all but the lowest SZAs, the number of effective measurements in glint mode permitted by the cloud-free probability in (f) must be further reduced by this rough factor of 2 as compared to the corresponding value for nadir given by (e).

ACPD

8, 20051–20112, 2008